

An Evaluation of Three Dimensional Diarthrodial Joint Contact Using Proximity Data
and the Finite Element Method

by

William L. Dunbar, Jr.

A Thesis Submitted to the
Graduate Faculty of Rensselaer Polytechnic Institute
in Partial Fulfillment of the
Requirements for the Degree of
MASTER OF SCIENCE

Approved:

Robert L. Spilker
Thesis Advisor

Rensselaer Polytechnic Institute
Troy, NY

April 1997
(for Graduation May 1997)

Table of Contents

List of Tables	iv
List of Figures	iv
Acknowledgments	v
Abstract	vii
Chapter 1: Introduction	1
Chapter 2: Mathematical and Computational Models of Biphasic Soft Tissues	6
2.1 Structure and Composition of Articular Cartilage	6
2.2 Mathematical Formulations: Linear Biphasic Theory with Contact Boundary Conditions	8
2.3 Finite Element Formulations of the Biphasic Governing Equations	11
2.3.1 Mixed Velocity-Pressure Formulation	11
2.3.2 Mixed-Penalty Contact Formulation	18
Chapter 3: Methods for Using Proximity Data in Diarthrodial Joint Contact Analysis ..	19
3.1 Joint Modeling and Proximity Data from Stereophotogrammetry	19
3.2 Load Partitioning in Biphasic Materials	20
3.2.1 Definition of Biphasic Load Partitioning Factor, ϕ^*	21
3.2.2 Derivation of Elastic Stress from Proximity Data	22
3.2.3 Derivation of Total Stress from Proximity Data	24
3.3 Numerical Algorithm for ϕ^* Calculation	25
3.3.1 Calculation of Elastic Stress from Proximity Data	27
3.3.2 Calculation of Total Stress from Proximity Data	30

Chapter 4: Validation Examples: Axisymmetric Contact Problems	32
4.1 Axisymmetric Validation Model Description	32
4.2 Finite Element Configurations	36
4.3 Results	37
4.3.1 Two-dimensional Validations	38
4.3.2 Comparison of 2D and 3D Results	46
Chapter 5: Summary and Conclusions	50
Bibliography	54

List of Tables

Table 4.1 Canonical Joint Dimensions	34
Table 4.2 Canonical Joint Material Property Sets	35
Table 4.3 Canonical Joint Material Configurations	35
Table 4.4 Canonical Joint Analysis Cases.....	36
Table 4.5 Average ϕ^* values for 2D contact and 3D proximity analysis cases	45

List of Figures

Figure 2.1 Organization of the collagen matrix of articular cartilage.	7
Figure 2.2 Ultra-scale (10^{-8} - 10^{-6} m) cartilage depiction	7
Figure 2.3 10-node tetrahedral element.....	17
Figure 3.1 Surface normals on contacting bodies	23
Figure 3.2 v - p 10-node tetrahedral element.....	26
Figure 3.3 Tangent-normal coordinate system for an element.....	28
Figure 4.1 Canonical Joint Model Configuration.....	33
Figure 4.2 Representative FE Meshes of Canonical Joint Model for 2D Contact (left) and 3D Proximity (right) Analyses.....	37
Figure 4.3 Normal displacement, total proximity, and layer assigned proximity vs. radial position at $t=0.1$ s	40
Figure 4.4 Normal elastic stress for contact and proximity analyses vs. radial position at the contact surface at $t=0.1$ s	42
Figure 4.5 Normal total stress for contact and proximity analyses vs. radial position at the contact surface at $t=0.1$ s	44
Figure 4.6 2D (upper) and 3D (lower) normal solid strain for analysis case A12	47
Figure 4.7 2D (upper) and 3D (lower) solid strain on z-r face for analysis case A12	48

Acknowledgments

I first need to thank my thesis advisor, Dr. Robert Spilker. It has been his guidance, encouragement and patience that has allowed me to complete this body of work. Despite his full schedule he was always available to help a struggling graduate student in any capacity he could.

I next need to acknowledge all those who made significant technical contributions to this thesis. First Drs. Peter Donzelli and Edgard Almeida for the use of their finite element codes. This work would not have been possible without their help. Also, Dr. Gerard Ateshian and the Orthopaedic Research Lab at Columbia University for their clinical input and stereophotogrammetry data. Finally, Bob O’Bara and Rob Michaloski for their contributions in turning the SPG data into the models I needed for my work.

I have been lucky to enjoy many great friendships with my colleagues in the Computational Biomechanics Lab, here at Rensselaer. Pete Donzelli, Edgard Almeida, Sharon Tabolt, Rob Michaloski, Elena Kenderova and Kerem Un have all been fantastic friends. They made being in the lab an enjoyable experience.

I certainly could not have succeeded without the support of my family. When I was down about the progress of this thesis they picked me back up and helped me to the finish line. Everyone should be as lucky as I am to be surrounded by such wonderful people. I also can’t discount Tupper’s help. It’s impossible to describe how he is able to understand my moods and cheer me up when need be.

Last, but certainly not least, my fiancée Jana. She is the driving force in my life and it was when I realized that I was doing this thesis as much for her as for myself that I became truly motivated to finish the work.

Abstract

In an effort to investigate mechanical response in hydrated soft tissues of human diarthrodial joints to physiological levels of loading, a method to simulate three-dimensional (3D) contact between opposing cartilage layers has been developed and is presented here. The method utilizes the linear biphasic theory to represent soft hydrated tissues as a continuum, solid modeling techniques to generate 3D models of tissue layers, penetration of opposing tissue layers to approximate contact loads, and the finite element method to solve the governing biphasic equations for the 3D response of the contacting tissue layers. Kinematic information describing a joint articulation is measured while the cartilage layers are deformed under physiological loads. The joint is disarticulated, allowing the soft tissue layers to relax, to ascertain the geometric properties of the cartilage layers via stereophotogrammetry (SPG). Solid models of the relaxed layers are generated and representations of the joint are assembled using the previously collected kinematic data. Contacting cartilage layers in the resulting joint model will overlap; the magnitude and distribution of the overlap is calculated using the solid modeler and called “proximity data”. Proximity data is assumed to represent deformation of the contacting surfaces and is translated via the biphasic governing equations into boundary conditions for finite element analysis. Since the tissues are multi-phase materials, a method for partitioning the total load between phases is developed. Values for time-dependent quantities such as stress, strain and fluid velocity are then calculated via a 3D biphasic finite element analysis. In this study, results for

canonical geometric configurations are compared with results from independent biphasic contact analyses to show that the proximity method yields a good approximation to contact.

Chapter 1: Introduction

Diarthrodial joints in the human body are capable of supporting high levels of mechanical load over the span of decades. However, degenerative joint diseases affect millions of people every year, preventing them from carrying out normal everyday activities. In order to battle diseases such as osteoarthritis (OA), we must first understand how diarthrodial joint components behave and interact with one another in response to physiological levels of load under both healthy and pathological conditions. These interactions are both chemical and mechanical, making them difficult to interpret. Researchers have been pondering these interactions, and how they relate to total joint function, for almost a hundred years. While much has been learned in this time-span, it has been the recent advent of high performance computers that has allowed us to begin to simulate joint mechanics and investigate the underlying details of the problem. This thesis combines many of the research techniques that have been recently developed into a method to study the mechanics of diarthrodial joints.

In our efforts to accurately represent diarthrodial joint mechanics we have developed or incorporated methods to measure joint geometry and kinematics, represent the tissues as continua, construct 3D solid models of tissue layers, solve the continuum problems using finite element methods, and visualize the time-dependent results. Recent advances in medical imaging, such as stereophotogrammetry (destructive) [6] and high resolution MRI (non-destructive), allow us to generate accurate geometric models of biological structures. Studies on the mechanical and material properties of biological

materials, specifically cartilage, have yielded accurate constitutive models, such as the biphasic [18] and triphasic [14] theories. These models can be used in conjunction with the geometric representations to quantify the mechanics of soft tissues through both analytical and numerical procedures. The numerical methods are constantly improving as the ability to do large-scale computing becomes more viable. These components lead to complete and accurate models of diarthrodial joints that can be used in numerous ways, such as computer simulated or computer aided surgery, prosthetic design, or investigation of degenerative joint diseases. Unfortunately, the type of high performance computing necessary to fully implement some of these investigative techniques still has limited availability. The study presented here is motivated by the immediate need for computationally feasible techniques that can be widely used to study the 3D mechanical response of soft tissue layers in contact in diarthrodial joints.

The soft tissue layers of diarthrodial joints are only a few millimeters thick, yet they can support the types of loads that are generated during physical activities, such as running, for the life-span of a person. Human-engineered materials can support similar levels of load, but not for the duration of time (decades) that physiological materials can. This is partly due to the fact that cartilage is a living material and can replenish itself, but is more directly due to the mechanical properties of hydrated tissues. Specifically, the multi-phase nature of cartilage and the corresponding lubrication mechanisms [19] make cartilage one of the most efficient bearing materials known. While biological materials have been mathematically represented using various continuum models and constitutive laws, the appropriate laws must reasonably

represent the physical behavior of the material. For the present application the biphasic theory of Mow et al. [18] will be used as it has been shown to be robust and accurate for analytical and numerical analyses of diarthrodial joint cartilage mechanics. In this initial study, which is focused on the method to define loads on contacting biphasic layers, the linear form of the biphasic theory is used. The method can be extended to nonlinear theories in future studies.

In order to perform any analysis of cartilage, geometric models are needed. The methods in this study are tested using simple canonical geometric models, but will also apply to more complicated physiological models derived from stereophotogrammetry or other imaging technologies, such as MRI. This is important, for in order to draw clinically relevant conclusions from our analyses we must have models based on real joint structures. In parallel efforts, SPG (and other) data generated by our collaborators at the Orthopedic Research Laboratory at Columbia University is being used to construct accurate 3D models of diarthrodial joints and their tissue layers which can then be subjected to 3D biphasic analysis. Once accurate solid models have been generated and solved they can be used in numerous ways (visualization, prosthetic design, finite element analysis, etc.) to aid clinicians in their treatment of patients.

Finite element analysis is a field that has grown rapidly in recent years. As computers become more powerful, researchers develop computational tools and become more capable of analyzing complex structures and in turn engineering better products and unlocking physical mysteries. In biomedical engineering, numerical methods such as finite element analysis has given researchers a better understanding of the inner

mechanical workings of the human body. Specific to this study, much progress has been made in the analysis of soft tissues using the biphasic theory. Various finite element formulations have been developed and implemented [28; 29; 30; 4; 5; 10] for different situations, such as large deformation and biphasic contact. In a later chapter, the two formulations that are used in this study will be presented.

One of the more computationally demanding and fundamental aspects of diarthrodial joint analysis is the continuum contact that exists between the weight bearing soft tissue layers of a joint. The mechanical behavior of diarthrodial joints is dictated by this contact as forces are transmitted from one side of the joint to the other through the soft tissue layers, such as cartilage and menisci. Numerical analyses of three dimensional, multi-phase contact models are complicated and, as previously mentioned, computationally demanding. In an effort to simulate diarthrodial joint function, while avoiding some of the computational demands of fully 3D contact analysis, a method will be presented here that approximates the soft tissue contact mechanics by utilizing available geometric data and the biphasic theory to replace opposing tissue layers with surface tractions that embody the contact conditions on one layer. In this way, the size and complexity of the problem is reduced to a series of biphasic analyses on individual 3D tissue layers, making it easier to analyze the mechanical state of soft tissues in physiological situations. This will hopefully lead to insights into diarthrodial joint function under physiological conditions.

Chapter 2 will provide a summary of the linear biphasic theory for soft hydrated tissues and the finite element formulations of the theory that are used in this study.

Chapter 3 describes the method for simulating diarthrodial joint contact using proximity data. Chapter 4 presents validation examples for the method, where axisymmetric problems are analyzed in 3D using proximity data and compared with the solution computed from an independent 2D contact analysis. In these examples parameters such as material properties and joint congruency are varied to show that the method works for a wide range of problems. Finally, Chapter 5 draws conclusions about the method and makes recommendations for future work.

Chapter 2: Mathematical and Computational Models of Biphase Soft Tissues

2.1 Structure and Composition of Articular Cartilage

The articular cartilage that lines the diarthrodial joints of the human body is a matrix of biological materials, including collagen fibers (15 to 22% of the wet weight), proteoglycans (4 to 7%), interstitial fluid (60 to 85%) and others [17; 21; 20]. These constituents can be classified as either solid or fluid, allowing the overall tissue to be characterized as a two-phase continuum. The solid constituents, mainly collagen and proteoglycan aggregates, compose a matrix that is arranged in such a way as to make articular cartilage structurally stable. Near the articular surface the collagen fibers tend to be arranged parallel to the surface, in the middle zone of cartilage the collagen is randomly oriented, and in the deep zone the fibers are aligned perpendicular to the subchondral bone. The large proteoglycan aggregates are restrained within this matrix and the interstitial water is able to flow in and around the solid constituents. Figures 2.1 and 2.2 depict cartilage as it is described above on the micro (10^{-7} - 10^{-4} m) and ultra (10^{-8} - 10^{-6} m) scales, respectively [20].

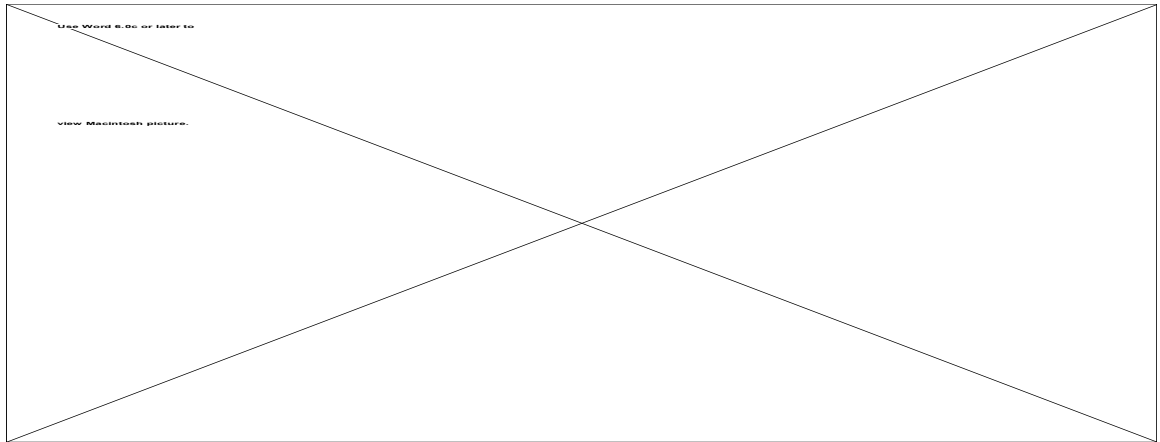


Figure Chapter 2: .1 Organization of the collagen matrix of articular cartilage.
Figure adapted from Mow et. al [20]

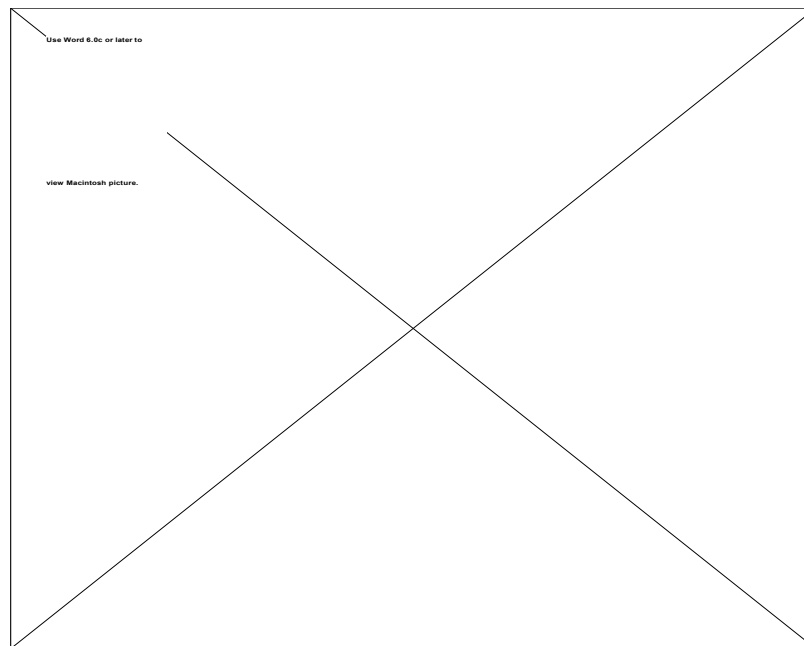


Figure Chapter 2: .2 Ultra-scale (10^{-8} - 10^{-6} m) cartilage depiction
Figure adapted from Mow et. al [20]

From the above descriptions of the structure of articular cartilage, one can conclude that it is a structurally anisotropic material. Cartilage is also known to be inhomogeneous. The content of both the collagen and the interstitial fluid decrease with

depth while the proteoglycan content increases towards the deep zone [20]. Finally, due to the large magnitude of loading (several times body weight in knees and hips [20]) that cartilage experiences in weight bearing joints, it is known that large deformation exists in cartilage. All of these facts must be taken into consideration when developing a mathematical model of the mechanical behavior of cartilage.

2.2 Mathematical Formulations: Linear Biphasic Theory with Contact Boundary Conditions

As just discussed, articular cartilage is composed of multiple phases, is structurally anisotropic and is inhomogenous, making it a difficult material to model mathematically. In this study, the linear biphasic theory [18] is used to model cartilage, which will be approximated as being isotropic and homogenous. However, nothing will be done to preclude the inclusion of an anisotropic or inhomogenous model in future studies. The governing equations of the linear biphasic theory for hydrated soft tissues are presented in this section. The biphasic theory assumes that the tissue is a continuum consisting of an incompressible solid and an incompressible, inviscid fluid phase. It is the drag created by the relative movement of the fluid through the solid matrix that gives the tissue its viscoelastic properties. In the following equations, the superscripts s and f refer to the solid and fluid phases, respectively.

From a consideration of mass conservation for a fixed spatial volume the continuity equation for the mixture is derived:

$$\left(\phi^f v_i^f + \phi^s v_i^s \right)_{,j} = 0 , \quad (2.1)$$

where ϕ , $\alpha=s,f$, is the solid or fluid content, \mathbf{v}^α , $\alpha=s,f$, is solid or fluid velocity and the comma (,) denotes spatial differentiation. There are momentum equations for each phase:

$$\sigma_{ij,j}^\alpha + \Pi_i^\alpha = 0; \quad \alpha = s, f, \quad (2.2)$$

where the body force term, Π_i^α , is related to the relative flow of the fluid and solid phases, and σ^α is the stress in the α phase. Finally, energy conservation leads to the following set of constitutive equations, one for each phase and one for the body force:

$$\sigma_{ij}^s = -\phi^s p \delta_{ij} + \sigma_{ij}^E \quad (2.3)$$

$$\sigma_{ij}^f = -\phi^f p \delta_{ij} \quad (2.4)$$

$$\Pi_i^s = -\Pi_i^f = p \phi_{,i}^s + K(v_i^f - v_i^s) \quad (2.5)$$

where $\sigma_{ij}^E = C_{ijkl} \epsilon_{kl}^s$ is the elastic part of the solid stress due to deformation (the familiar Hooke's Law from elasticity), p is pressure, and K is the diffusive drag coefficient, which is related to the tissue permeability, κ , by the expression [15]:

$$K = \frac{(\phi^f)^2}{\kappa}. \quad (2.6)$$

The fourth-rank tensor, \mathbf{C} , can admit any type of material symmetry, isotropic or anisotropic. While the continuum is assumed to be isotropic here, there is recent evidence suggesting that a transversely isotropic model is more appropriate for articular cartilage [7; 9]. Also, κ is assumed to be constant in this study, although it could be assumed to be dependent upon the solid strain [11]. Nothing will be done in the

following chapters to preclude the use of an anisotropic material model or strain-dependent permeability with the method being developed.

To solve biphasic boundary-initial value problems, we must also have boundary and initial conditions. They are as follows:

$$u_i^s = \bar{u}_i^s \text{ on } \Gamma_{u_i^s} \quad (2.7)$$

$$v_i^\alpha = \bar{v}_i^\alpha \text{ on } \Gamma_{v_i^\alpha}; \quad \alpha = s, f \quad (2.8)$$

$$\sigma_{ij}^\alpha n_j = \bar{t}_i^\alpha = \tilde{t}_i^\alpha \text{ on } \Gamma_{t_i^\alpha}; \quad \alpha = s, f \quad (2.9)$$

where $(\bar{})$ indicates a prescribed value of () . These conditions correspond to prescribed solid displacement (u^s), solid or fluid velocity (v^α , $\alpha=s,f$), and solid or fluid traction (t^α , $\alpha=s,f$), respectively. Note from the constitutive relation (2.4) that the prescribed fluid traction in Eqn. (2.9) is $\tilde{t}_i^f = \phi^f \bar{p} n_i$. The problems to be solved in this study arise from the contact between two biphasic tissue layers. Therefore, in addition to the above boundary conditions there are also the boundary conditions between two contacting biphasic bodies, denoted with superscripts A and B, [12] which are important for this study:

$$v_i^{sA} n_i^A + v_i^{sB} n_i^B = 0, \quad (2.10)$$

$$\left(\phi^{fA} v_i^{fA} + \phi^{sA} v_i^{sA} \right) n_i^A + \left(\phi^{fB} v_i^{fB} + \phi^{sB} v_i^{sB} \right) n_i^B = 0, \quad (2.11)$$

$$p^A - p^B = 0, \quad (2.12)$$

$$\sigma_{ij}^{EA} n_j^A - \sigma_{ij}^{EB} n_j^B = 0. \quad (2.13)$$

Physically the boundary conditions (2.10) - (2.13) represent two kinematic conditions, continuity of normal solid velocity and continuity of normal relative flow, and two

kinetic conditions, continuity of pressure and continuity of normal elastic traction, respectively.

The finite element method [13; 32] may be used to solve the above equations over complicated spatial domains by discretizing the domain into smaller parts (elements) over which unknown field variables are approximated, thus approximating the equations over these smaller domains. The result is a system of equations (linear first order equations for the linear biphasic problem) that can be solved for the unknown values of the field variables at the FE nodes. Special types of FE formulations, such as penalty and mixed methods, are required to obtain accurate results for problems containing constraints and multiple field variables, as the above biphasic equations do. Such formulations for these biphasic equations of soft hydrated tissues have been developed within our group [28; 29; 30]; the two that will be used in this study are discussed below.

2.3 Finite Element Formulations of the Biphasic Governing Equations

2.3.1 Mixed Velocity-Pressure Formulation

The mixed velocity-pressure (v - p) formulation is characterized by the elimination of fluid velocity in the governing equations. This is done by manipulating equations (2.1) - (2.5) while assuming that the mixture is saturated, i.e. $\phi^f + \phi^s = 1$ and thus $\phi_{,i}^f = -\phi_{,i}^s$. The fluid constitutive equation, (2.4), and the diffusive drag equation, (2.5), are substituted into the fluid momentum equation, (2.2), to arrive at;

$$\left(v_i^f - v_i^s\right) = \frac{-\kappa}{\phi^f} p_{,i} . \quad (2.14)$$

The fluid velocity is eliminated by noting that the continuity equation, (2.1), can be expressed as;

$$\left(\phi^f v_i^f + \phi^s v_i^s + \left(\phi^f v_i^s - \phi^s v_i^f\right)\right)_{,i} = 0 . \quad (2.15)$$

For a saturated mixture Eqn (2.15) can be rewritten using equation (2.14) as

$$\left(v_i^s - \kappa p_{,i}\right)_{,i} = 0 . \quad (2.16)$$

Next, the diffusive drag equations, (2.5), can be rewritten using Eqn (2.14) and (2.6) as:

$$\Pi_i^s = -\Pi_i^f = p\phi_{,i}^s + K\left(v_i^f - v_i^s\right) = p\phi_{,i}^s - \phi^f p_{,i} , \quad (2.17)$$

Using this result with the constitutive relations (2.3) and (2.4) makes the momentum equations, (2.2);

$$\begin{aligned} -\phi^s p_{,i} + \sigma_{ij,j}^E - \phi^f p_{,i} &= 0 \\ -\phi^f p_{,i} + \phi^f p_{,i} &= 0 \end{aligned} . \quad (2.18)$$

The first equation in (2.18) may be simplified, while the second equation is trivial.

This results in a system of equations that has solid velocity and pressure (a vector and a scalar) as field variables, as opposed to other methods that have solid and fluid velocities (two vectors) as their field variables. This velocity-pressure type of formulation has been used in mixture problems (for both soil mechanics and biomechanics) by [26; 23; 24; 31; 16]; the variation of it that is presented here was developed by Almeida [1; 5; 4; 3; 2]. These formulations have been shown to give accurate results and are also useful in reducing the number of degrees of freedom, and

thus computational demand, for a given problem by replacing the vector fluid velocity with the scalar pressure as a field variable.

The field variables in the governing equations are now solid displacement (velocity) and pressure. Therefore, the boundary conditions (2.7) - (2.9) must be altered as follows: there are no longer any conditions on the fluid velocity; pressure may be prescribed as an essential condition; and the prescribed fluid traction is replaced by a prescribed fluid flux, \bar{Q} . The boundary conditions are given by the following:

$$\bar{Q} = -(\kappa p_{,i})n_i = \phi^f(v_i^f - v_i^s)n_i \text{ on } \Gamma_Q \quad (2.19)$$

$$u_i^s = \bar{u}_i^s \text{ on } \Gamma_{u_i^s} \quad (2.20)$$

$$v_i^s = \bar{v}_i^s \text{ on } \Gamma_{v_i^s} \quad (2.21)$$

$$p = \bar{p} \text{ on } \Gamma_p \quad (2.22)$$

$$\sigma_{ij}^{Tot} n_j = t_i^{Tot} = \bar{t}_i^{Tot} \text{ on } \Gamma_{t_i^s} \quad (2.23)$$

As before, $(\bar{\cdot})$ indicates a prescribed quantity. The superscript *Tot* refers to total values (e.g. $\sigma_{ij}^{Tot} = \sigma_{ij}^s + \sigma_{ij}^f$). For contact analyses, the contact boundary conditions (2.10) - (2.13) would also need to be rewritten. However, since these boundary conditions will not be used for this v - p formulation, they are not rewritten here.

For the v - p formulation, a weighted residual statement is formed from the altered versions of the continuity equation, (2.16), and the linear momentum equations, (2.18), as well as the natural boundary conditions, (2.19) and (2.23):

$$\begin{aligned}
& \int_{\Omega} w_i (\sigma_{ij,j}^E - p_{,i}) d\Omega + \int_{\Omega} q (v_i^s - \kappa p_{,i})_{,i} d\Omega \\
& + \int_{\Gamma_t} w_i (t_i^{Tot} - \bar{t}_i^{Tot}) d\Gamma - \int_{\Gamma_Q} q (\bar{Q} + (\kappa p_{,i}) n_i) d\Gamma = 0,
\end{aligned} \tag{2.24}$$

where Ω is the spatial volume, Γ_t is a traction boundary and Γ_Q is a flow boundary. The weighting functions w_i (vector) and q (scalar) are arbitrary, admissible functions. Application of the Divergence Theorem will reduce the order of differentiation on the following three integrals:

$$\begin{aligned}
\int_{\Omega} w_i \sigma_{ij,j}^E d\Omega &= \int_{\Gamma} w_i \sigma_{ij}^E n_j d\Gamma - \int_{\Omega} w_{(i,j)} \sigma_{ij}^E d\Omega \\
\int_{\Omega} w_i p_{,i} d\Omega &= \int_{\Gamma} w_i p n_i d\Gamma - \int_{\Omega} w_{i,i} p d\Omega \\
\int_{\Omega} q \kappa p_{,ii} d\Omega &= \int_{\Gamma} q \kappa p_{,i} n_i d\Gamma - \int_{\Omega} q_{,i} \kappa p_{,i} d\Omega
\end{aligned} \tag{2.25}$$

Noting that the total boundary, Γ , is comprised of the sub boundaries, $\Gamma_Q, \Gamma_t, \Gamma_p, \Gamma_v^s$ ($\Gamma = \Gamma_Q + \Gamma_t + \Gamma_p + \Gamma_v^s$) Eqn (2.25) is substituted into (2.24) and boundary terms are canceled to obtain the v - p weak form:

$$\begin{aligned}
& \int_{\Omega} w_{(i,j)} \sigma_{ij}^E d\Omega - \int_{\Omega} w_{i,i} p d\Omega - \int_{\Omega} q v_{i,i}^s d\Omega - \int_{\Omega} q_{,i} \kappa p_{,i} d\Omega \\
& - \int_{\Gamma_t} w_i \bar{t}_i^{Tot} d\Gamma - \int_{\Gamma_Q} q \bar{Q} d\Gamma = 0
\end{aligned} \tag{2.26}$$

For the finite element method, the domain Ω is subdivided into elements and the weak form (2.26) is rewritten as a sum over these elements in matrix/vector form;

$$\begin{aligned}
& \sum_n \left\{ \int_{\Omega_n} (\nabla \mathbf{w})_{sym}^T \mathbf{C} (\nabla \mathbf{u})_{sym} d\Omega - \int_{\Omega_n} (\nabla \mathbf{w})_{sym}^T \mathbf{m}^T p d\Omega - \int_{\Omega_n} q (\nabla \mathbf{v}^s)_{sym} \mathbf{m} d\Omega \right. \\
& \left. - \int_{\Omega_n} (\nabla q) \kappa (\nabla p) d\Omega - \int_{\Gamma_t} \mathbf{w}^T \bar{\mathbf{t}}^{Tot} d\Gamma - \int_{\Gamma_Q} q \bar{Q} d\Gamma \right\} = 0
\end{aligned} \tag{2.27}$$

where \mathbf{m} represents the Kronecker delta and $\boldsymbol{\sigma}^E$ has been substituted for in terms of the solid strain, $\boldsymbol{\varepsilon}^s = (\nabla \mathbf{u}^s)_{sym}$, where $(\)_{sym}$ denotes the symmetric part of the gradient of solid displacement (\mathbf{u}^s). Interpolations for the field variables and weighting functions are defined in the following forms:

$$\mathbf{u}^s = \mathbf{N} \mathbf{d}_n^s; \quad \mathbf{v}^s = \mathbf{N} \mathbf{v}_n^s; \quad p = \mathbf{N}_p \mathbf{p}_n, \quad (2.28)$$

$$\mathbf{w} = \mathbf{N} \mathbf{w}_n; \quad q = \mathbf{N}_p \mathbf{q}_n. \quad (2.29)$$

where the \mathbf{N} and \mathbf{N}_p are shape functions and \mathbf{d} , \mathbf{v}_n , \mathbf{p}_n , \mathbf{w}_n and \mathbf{q}_n are vectors of nodal quantities. In the same form, interpolations for the gradients of \mathbf{w} , \mathbf{v} , \mathbf{u} , p and q are derived:

$$\begin{aligned} (\nabla \mathbf{u}^s)_{sym} &= (\nabla \mathbf{N})_{sym} \mathbf{d}_n^s = \mathbf{D}_\varepsilon \mathbf{d}_n^s; \quad (\nabla \mathbf{v}^s)_{sym} = (\nabla \mathbf{N})_{sym} \mathbf{v}_n^s = \mathbf{D}_\varepsilon \mathbf{v}_n^s \\ \nabla p &= (\nabla \mathbf{N}_p) \mathbf{p}_n = \mathbf{D}_p \mathbf{p}_n \\ (\nabla \mathbf{w})_{sym} &= (\nabla \mathbf{N})_{sym} \mathbf{w}_n = \mathbf{D}_\varepsilon \mathbf{w}_n; \quad \nabla q = (\nabla \mathbf{N}_p) \mathbf{q}_n = \mathbf{D}_p \mathbf{q}_n \end{aligned} \quad (2.30)$$

Substituting Eqns. (2.28) - (2.30) into the finite element weak form, Eqn. (2.26), and pulling the nodal coefficients of the weighting functions and the field variables out of the integrals gives

$$\begin{aligned} \sum_n \{ & \mathbf{w}_n^T \int_{\Omega_n} \mathbf{D}_\varepsilon^T \mathbf{C} \mathbf{D}_\varepsilon d\Omega \mathbf{d}_n^s - \mathbf{w}_n^T \int_{\Omega_n} (\mathbf{m} \mathbf{D}_\varepsilon)^T \mathbf{N}_p d\Omega \mathbf{p}_n \\ & - \mathbf{q}_n^T \int_{\Omega_n} \mathbf{N}_p^T (\mathbf{m} \mathbf{D}_\varepsilon) d\Omega \mathbf{v}_n^s - \mathbf{q}_n^T \int_{\Omega_n} \mathbf{D}_p^T \kappa \mathbf{D}_p d\Omega \mathbf{p}_n \\ & - \mathbf{w}_n^T \int_{\Gamma_{r^s}} \mathbf{N}^T \bar{\mathbf{t}}^{Tot} d\Gamma - \mathbf{q}_n^T \int_{\Gamma_Q} \mathbf{N}_p^T \bar{Q} d\Gamma \} = 0 \end{aligned} \quad (2.31)$$

From (2.31) element matrices can be identified as

$$\mathbf{a} = \int_{\Omega_n} (\mathbf{m} \mathbf{D}_\varepsilon)^T \mathbf{N}_p d\Omega \quad (2.32)$$

$$\mathbf{k}_n = \int_{\Omega_n} \mathbf{D}_\varepsilon^T \mathbf{C} \mathbf{D}_\varepsilon d\Omega \quad (2.33)$$

$$\mathbf{k}_p = \int_{\Omega_n} \mathbf{D}_p^T \mathbf{K} \mathbf{D}_p d\Omega \quad (2.34)$$

$$\mathbf{f}_n^{Tot} = \int_{\Gamma_i} \mathbf{N}^T \bar{\mathbf{t}}^{Tot} d\Gamma \quad (2.35)$$

$$\mathbf{f}_Q = \int_{\Gamma_Q} \mathbf{N}_p \bar{Q} d\Gamma \quad (2.36)$$

which gives the resulting matrix form:

$$\begin{aligned} & \sum_n \left(\begin{bmatrix} \mathbf{w}_n^T & \mathbf{q}_n^T \end{bmatrix} \begin{bmatrix} \mathbf{0} & -\mathbf{a} \\ -\mathbf{a}^T & \mathbf{k}_p \end{bmatrix} \begin{Bmatrix} \mathbf{v}_n^s \\ \mathbf{p}_n \end{Bmatrix} \right) + \sum_n \left(\begin{bmatrix} \mathbf{w}_n^T & \mathbf{q}_n^T \end{bmatrix} \begin{bmatrix} \mathbf{k}_n & \mathbf{0} \\ \mathbf{0} & \mathbf{0} \end{bmatrix} \begin{Bmatrix} \mathbf{d}_n^s \\ \mathbf{p}_n \end{Bmatrix} \right) \\ & = \sum_n \left(\begin{bmatrix} \mathbf{w}_n^T & \mathbf{q}_n^T \end{bmatrix} \begin{Bmatrix} \mathbf{f}_n^{Tot} \\ \mathbf{f}_Q \end{Bmatrix} \right) \end{aligned} \quad (2.37)$$

Note that the overall matrices (comprised of the previously defined element matrices) in (2.37) are symmetric.

The spatially discretized form of the v - p formulation was derived and shown here to point out the field variables that are involved, as they will come into play while deriving the proximity method in the next chapter. Note from (2.37) that the solid velocity (\mathbf{v}^s) and pressure (\mathbf{p}) are the field variables and therefore may be applied as essential boundary conditions. The natural boundary conditions are in the forcing terms on the right hand side of (2.37) and are total traction (\mathbf{f}^{Tot}) and flux (\mathbf{f}_Q). In the next chapter a method will be derived which translates proximity data for a geometric model into an essential pressure boundary condition and a total traction natural boundary condition. These boundary conditions will then be used in the preceding v - p finite

element formulation to arrive at results that are comparable to a full 3D biphasic contact analysis.

The implementation of the v-p formulation that is used in this work utilizes a 10-node tetrahedral finite element to solve the above matrix equations. A representative element is depicted below. This is a mixed formulation and therefore a linear pressure field (nodes 1,3,4 & 2) and a quadratic velocity field (nodes 1-10) are imposed over the element. This means that the shape functions defined earlier in Eqns. (2.28) - (2.30) are linear for pressure (\mathbf{N}_p) and quadratic for solid displacement/velocity (\mathbf{N}).

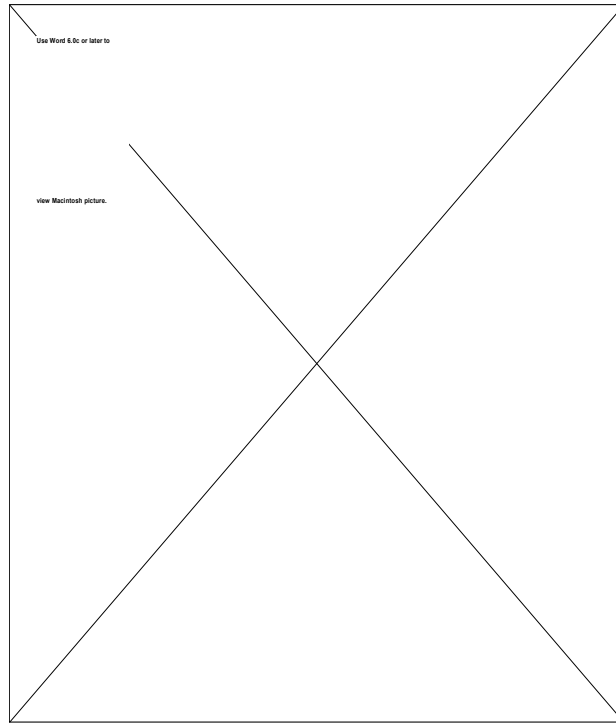


Figure Chapter 2: .3 10-node tetrahedral element

2.3.2 Mixed-Penalty Contact Formulation

In order to validate results from the v - p with proximity boundary conditions analyses, an independent biphasic contact analysis is needed. In this way, it can be verified that the solutions from the proximity method are accurate and in agreement with valid contact solutions. For the present study, the mixed-penalty biphasic contact formulation of Donzelli [8] is used. This formulation has been shown to converge to the correct contact solution and is therefore an appropriate choice for comparison with the methods derived in this thesis.

This formulation includes the contact boundary conditions of Eqns. (2.10) - (2.13) in the formation of its weighted residual statement. The contact conditions are enforced via Lagrange multipliers and an accurate contact solution is derived. The implementation of this formulation that is used in the present study is two dimensional. Therefore, all validations will be done using axisymmetric problems that can be solved in both two and three dimensions.

Chapter 3: Methods for Using Proximity Data in Diarthrodial

Joint Contact Analysis

In the biphasic finite element formulation of Chapter 2, applied loads are partitioned between the solid and fluid phases and defined in terms of applied tractions (Eqn. (2.9)), applied pressure (Eqn. (2.22)), or applied fluid flux (Eqn. (2.19)). In the present analysis, the load should also approximate the contact loads between two biphasic layers. However, the phase partitioning of a total applied load cannot be determined experimentally. In this chapter, a method is developed for determining the load partition which utilizes penetration data (proximity data) for contacting biphasic layers that is determined from stereophotogrammetry (SPG). This method then provides the correct biphasic boundary conditions for the finite element analysis.

3.1 Joint Modeling and Proximity Data from Stereophotogrammetry

Proximity data is defined in the following manner [27]. Kinematic data for a diarthrodial joint articulation is collected at quasi-static positions while the joint is still intact. During the articulation, the applied tendon and ligament forces result in deformation of the soft tissues of the joint. The joint is then disarticulated to reveal the articular cartilage surfaces. When the joint is dissected, the soft tissues that were deformed during the articulation relax (this will be referred to as the “undeformed” state). Stereophotogrammetry (SPG) is then used to measure the surface geometry of the undeformed cartilage layers and the underlying bone surfaces, providing

mathematical representations of the upper and lower tissue surfaces. When these surfaces are mathematically reassembled in space using the kinematic data from the articulation, the undeformed tissue layers will inter-penetrate due to the relaxation of the cartilage after dissection. This penetration is quantified using solid modeling techniques within commercial solid modeling software and is assumed to be a measure of the total articular cartilage deformation that occurred during the joint articulation. Therefore, the penetration, or proximity, data can be used to calculate estimates of solid strain or solid traction using the constitutive laws of Chapter 2. This will be utilized below to calculate a load partition in biphasic materials.

The SPG data gives surface representations for the cartilage layers of a joint. For finite element analysis these surface representations must be converted into solid models for which 3-D finite element meshes can be generated. Commercial solid modeling packages are used to create these solid models using algorithms described by O'Bara et. al [22] for converting SPG data into solid models. Once the 3-D solid is complete, Finite Octree© [25] is used to generate meshes of solid 10-node tetrahedral elements. These meshes are used with the v - p finite element formulation described in Chapter 2 and the proximity boundary conditions to be described below to produce realistic mechanical analyses of diarthrodial joints.

3.2 Load Partitioning in Biphasic Materials

As previously discussed, to correctly apply loading boundary conditions in biphasic analyses it is necessary to partition the load between the two phases. A method

is described below for calculating the partition between biphasic layers in contact using the biphasic governing equations of Chapter 2 and proximity data .

3.2.1 Definition of Biphasic Load Partitioning Factor, ϕ^*

In order to quantify how a load is divided between the volume phases, a load sharing parameter, ϕ^* , is defined over a contact interface. This parameter indicates the percentage of the total stress that is carried by the solid phase of the tissue (a ϕ^* value of 1 indicates that the load is fully supported by the solid phase). The parameter is defined in terms of normal surface tractions (Eqns. 1.9) as:

$$t_i^s n_i = \sigma_{ij}^s n_i n_j = \phi^* \sigma_{ij}^{Total} n_i n_j \quad (3.1a)$$

$$t_i^f n_i = \sigma_{ij}^f n_i n_j = (1 - \phi^*) \sigma_{ij}^{Total} n_i n_j \quad (3.1b)$$

where n is a surface unit normal, and the total stress normal to the surface is;

$$\sigma_{ij}^{Total} n_i n_j = \sigma_{ij}^s n_i n_j + \sigma_{ij}^f n_i n_j = -p n_i n_i + \sigma_{ij}^E n_i n_j. \quad (3.2)$$

To quantify ϕ^* , consider the following manipulation of Eqns. (3.1) & (3.2).

Solving Eqn. (3.2) for pressure, p , gives:

$$p n_i n_i = \sigma_{ij}^E n_i n_j - \sigma_{ij}^{Total} n_i n_j. \quad (3.3)$$

Substituting (3.3) into the constitutive equation for the solid stress, (2.3), yields

$$\sigma_{ij}^s n_i n_j = \phi^f \sigma_{ij}^E n_i n_j + \phi^s \sigma_{ij}^{Total} n_i n_j. \quad (3.4)$$

Solving Eqn. (3.1) for ϕ^* and utilizing Eqns. (3.3) and (3.4) gives the following equation for ϕ^* :

$$\boxed{\phi^* = \frac{\sigma_{ij}^s n_i n_j}{\sigma_{ij}^{Total} n_i n_j} = \phi^s + \phi^f \left(\frac{\sigma_{ij}^E n_i n_j}{\sigma_{ij}^{Total} n_i n_j} \right)}. \quad (3.5)$$

Using Eqn. (3.5) in conjunction with proximity data, the parameter ϕ^* can be calculated as next described.

3.2.2 Derivation of Elastic Stress from Proximity Data

To calculate ϕ^* in Eqn. (3.5), the normal elastic stress due to deformation of the solid phase, σ^E , which appears on the right hand side of Eqn. (3.5), will be calculated from the proximity data. Following classical continuum mechanics, the elastic stress is related to the solid strain, ϵ^s ;

$$\sigma_{ij}^E = C_{ijkl} \epsilon_{kl}^s \rightarrow \sigma_{ij}^E n_i n_j = C_{ijkl} \epsilon_{kl}^s n_i n_j, \quad (3.6)$$

which in turn is related to the deformation of the solid phase by:

$$\epsilon_{ij}^s = \frac{1}{2} (u_{i,j}^s + u_{j,i}^s) \equiv u_{(i,j)}^s, \quad (3.7)$$

where the comma (,) denotes differentiation, and the standard definition of the symmetric part of gradient is used on the right hand side of Eqn. 3.7 for notational convenience.

The SPG data and solid modeling operations yield the “total” proximity for a set of opposing layers which must be appropriately divided between the layers. If two bodies are in contact, their surface normals will be equal and opposite across the contact surface (see Figure 3.1);

$$n_i^A = -n_i^B = n_i. \quad (3.8)$$

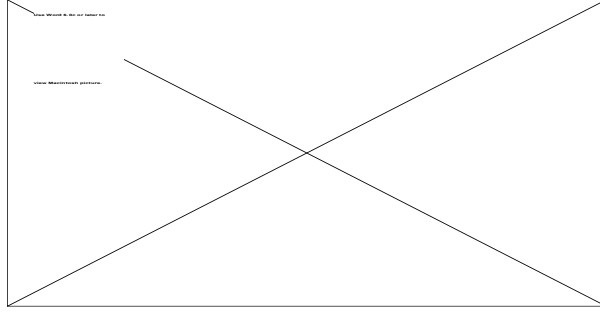


Figure Chapter 3: .1 Surface normals on contacting bodies

Once apportioned to a layer, the proximity is assumed to be equal to the solid deformation of that layer. With these assumptions the following expressions hold;

$$g_i^A = u_i^{s^A} = \alpha g_i^{Total} \quad (3.9a)$$

$$g_i^B = u_i^{s^B} = (1 - \alpha) g_i^{Total} \quad (3.9b)$$

$$g_i^{Total} = u_i^{s^A} + u_i^{s^B} = u_i^{s^{Total}} , \quad (3.9c)$$

where A and B denote the two opposing bodies, g_i is the Cartesian component of the proximity vector (note that the proximity vector is by definition normal to the surface), and α is the proximity partitioning parameter representing the fraction of the proximity ascribed to side A . With these definitions and Eqns. (3.6) and (3.7), σ^E can be calculated. However, the parameter α must first be determined.

To calculate α , the contact boundary condition corresponding to continuity of normal elastic traction (Eqn. (2.13)) is used. This contact condition states that the normal component of the elastic portion of the solid stress is continuous between two contacting biphasic bodies, A and B ,

$$\sigma_{ij}^{E^A} n_i n_j = \sigma_{ij}^{E^B} n_i n_j . \quad (3.10)$$

Equation (3.6) defines the part of the solid stress due to deformation for a linear isotropic solid phase. Substituting this definition and Eqn. (3.7) into (3.10) yields:

$$\frac{1}{2}C_{ijkl}^A(u_{k,l}^{s^A} + u_{l,k}^{s^A})n_i n_j = \frac{1}{2}C_{ijkl}^B(u_{k,l}^{s^B} + u_{l,k}^{s^B})n_i n_j. \quad (3.11)$$

Finally, assuming that the proximity can be divided between layers and that the layer proximity is equal to the layer deformation, Eqns. (3.9) can be substituted into Eqn. (3.11), and the parameter α can be solved for:

$$\alpha = \frac{C_{ijkl}^B n_i n_j g_{(k,l)}^{Total}}{C_{ijkl}^A n_i n_j g_{(k,l)}^{Total} + C_{ijkl}^B n_i n_j g_{(k,l)}^{Total}}. \quad (3.12)$$

With this parameter, the elastic stress on each tissue layer can be calculated using Eqns. (3.6), (3.7) & (3.9). Referring back to Eqn. (3.5) for the parameter ϕ^* , the total normal surface traction, $\sigma_{ij}^{Tot} n_i n_j$, must be calculated next.

3.2.3 Derivation of Total Stress from Proximity Data

To calculate the total normal surface traction, it is first observed from biphasic contact finite element analyses (see Chapter 4) that the distributions of all normal traction quantities, including total traction, over the contact area can be normalized to the same distribution as the penetration data for short periods of time (1/10s of seconds). This observation leads to the expression:

$$\sigma_{ij}^{Total} n_i n_j = \gamma g_i^A n_i, \quad (3.13)$$

where γ is a proportionality constant between total traction and penetration distributions. In joint testing, the total force vector on a joint is likely to be known. Therefore, the total traction must be defined in terms of the total applied force, \mathbf{F}^{Total} ,

$$\int_{\Gamma^c} \sigma_{ij}^{Total} n_i n_j d\Gamma = |F_i^{Total}|, \quad (3.14)$$

where Γ^c is the contact surface. Equation (3.14) follows from considering that the kinematic data is collected at quasi-static positions; therefore the joint must be in static equilibrium (no motion) for each position used during collection of the data. Using Eqns. (3.13) and (3.14) γ can be calculated from the known proximity data and total force magnitude as:

$$\int_{\Gamma^c} \gamma g_i n_i d\Gamma = |F_i^{Total}| \rightarrow \gamma = \frac{|F_i^{Total}|}{\int_{\Gamma^c} g_i n_i d\Gamma}, \quad (3.15)$$

assuming that γ is constant in space over the contact surface (this assumption will be validated in Chapter 4 using biphasic contact solutions). Eqn. (3.13) can then be used to calculate the normal total traction at any point on the contact surface.

The derivations in Sections 3.2.2 and 3.2.3 give the necessary equations to calculate ϕ^* , defined by Eqn. (3.5). However, to quantify ϕ^* , numerical methods are needed to perform the necessary differentiation and integration over the complex 3D surfaces found in diarthrodial joints.

3.3 Numerical Algorithm for ϕ^* Calculation

In the development of the proximity method, proximity data has been treated as a continuous function, but it is actually calculated point-wise over a fixed grid imposed upon a model surface. To evaluate the expressions that were presented in the last section, continuous functions must be fit through the proximity data. These functions

can then be integrated and differentiated as needed (Eqns. (3.1) - (3.15)). This will be accomplished by using the shape functions of the 10-node tetrahedral meshes that will be used for finite element analysis of the concerned tissue layers. Therefore the loaded model surface is discretized into 6-node triangles (for instance, the face defined by nodes 1, 2 & 3 in Figure 3.2)

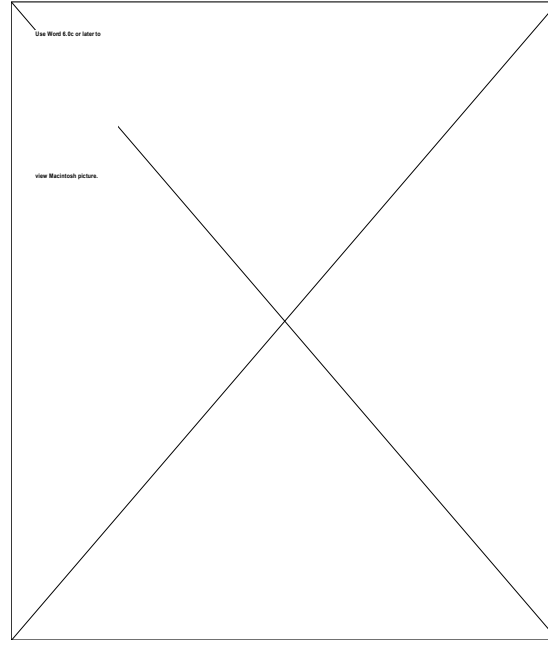


Figure Chapter 3: .2 v - p 10-node tetrahedral element

Using standard finite element 6-node shape functions for a face, continuous proximity functions can be derived as

$$g_i = \sum_{a=1}^6 N_a \xi_{ia}, \quad i = 1, 2, \quad (3.16)$$

where ξ_{ia} are the nodal values of the proximity components and N_a are quadratic finite element shape functions which can be defined in global (Cartesian) or local (triangular)

coordinates. The quadratic 6-node shape functions in triangular, or area, coordinates are:

$$\begin{aligned}
N_1 &= (2\xi_1 - 1)\xi_1 \\
N_2 &= (2\xi_2 - 1)\xi_2 \\
N_3 &= (2\xi_3 - 1)\xi_3, \\
N_4 &= 4\xi_1\xi_2 \\
N_5 &= 4\xi_2\xi_3 \\
N_6 &= 4\xi_1\xi_3
\end{aligned} \tag{3.17}$$

where ξ_i , $i = 1, 3$ are the triangular coordinates. For a full discussion of finite element shape functions, area coordinates, and numerical integration see [13; 32].

In the present implementation all of the following calculations are done at every finite element node on the loaded surface. However, since the final values of ϕ^* have small deviations over the contact surface, a scheme for choosing a subset of optimally located points could be derived, improving the overall efficiency of the calculations.

3.3.1 Calculation of Elastic Stress from Proximity Data

Assuming frictionless contact between the opposing tissue layers, components of stress that are tangential to the contact surface can be ignored. It is therefore convenient to define a tangent-normal coordinate system (t_1, t_2, n) for each element which has a face on the loaded contact surface (see Figure 3.3).

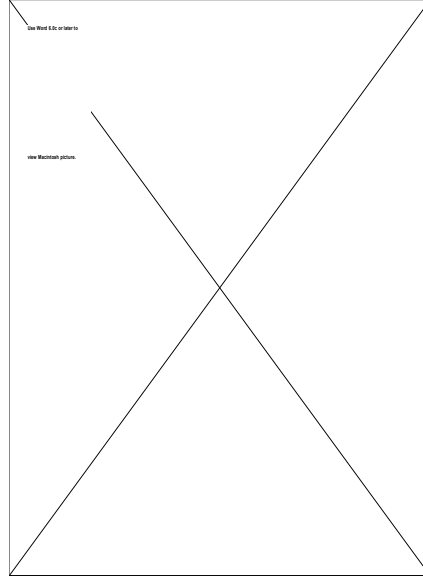


Figure Chapter 3: .3 Tangent-normal coordinate system for an element

Using this tangent-normal system, the stress-strain law (Eqn. (3.6)) for an isotropic solid can be written:

$$\begin{Bmatrix} \sigma_{t_1 t_1}^E \\ \sigma_{t_2 t_2}^E \\ \sigma_{nn}^E \\ \sigma_{t_2 n}^E \\ \sigma_{t_1 n}^E \\ \sigma_{t_1 t_2}^E \end{Bmatrix} = \begin{bmatrix} 2\mu + \lambda & \lambda & \lambda & 0 & 0 & 0 \\ \lambda & 2\mu + \lambda & \lambda & 0 & 0 & 0 \\ \lambda & \lambda & 2\mu + \lambda & 0 & 0 & 0 \\ 0 & 0 & 0 & \mu & 0 & 0 \\ 0 & 0 & 0 & 0 & \mu & 0 \\ 0 & 0 & 0 & 0 & 0 & \mu \end{bmatrix} \begin{Bmatrix} \varepsilon_{t_1 t_1}^s \\ \varepsilon_{t_2 t_2}^s \\ \varepsilon_{nn}^s \\ \varepsilon_{t_2 n}^s \\ \varepsilon_{t_1 n}^s \\ \varepsilon_{t_1 t_2}^s \end{Bmatrix}, \quad (3.18)$$

where λ and μ are Lamé's constants. The expression for the normal elastic stress component can be obtained from Eqn. (3.18);

$$\sigma_{nn}^E = \lambda \varepsilon_{t_1 t_1}^s + \lambda \varepsilon_{t_2 t_2}^s + (2\mu + \lambda) \lambda \varepsilon_{nn}^s. \quad (3.19)$$

In order to calculate the normal elastic stress component in Eqn. (3.19), the three strains on the right hand side are needed. These will be derived from the solid deformation in the tissue, assumed here to be proportional to the proximity data (Eqns. (3.9)).

Following Section 3.2.2, the proximity layer partitioning factor, α , is used to apportion the proximity data between opposing layers.

The calculation of α , Eqn. (3.12) requires data from both contacting tissue layers, and thus introduces a level of complexity that may not be necessary if the intention is to create a model and solution for only one of the layers. Therefore, in the present analysis Eqn. (3.12) is reduced to one dimension in order to get a simplified expression for α ;

$$\alpha = \frac{C_{ijkl}^B n_i n_j g_{(k,l)}^{Total}}{C_{ijkl}^A n_i n_j g_{(k,l)}^{Total} + C_{ijkl}^B n_i n_j g_{(k,l)}^{Total}} \rightarrow \alpha = \frac{1}{\left(1 + \frac{H_A^A}{H_A^B}\right)}, \quad (3.19)$$

where H_A is the aggregate modulus and is defined as:

$$H_A = (2\mu + \lambda). \quad (3.20)$$

The solid strain, Eqn. (3.7), can now be calculated from the interpolated proximity data, Eqn. (3.16), and the parameter α .

Since the proximity data is only defined over the contact surface, and not below the contact surface, a procedure to calculate the normal component of strain in Eqn. (3.19) is needed. For this method, the normal strain at the contact surface will be approximated by calculating the change in tissue layer thickness divided by the original tissue layer thickness at each finite element node on the contact surface:

$$\varepsilon_{nn}^s = \frac{\delta h}{h_0} = \frac{g_{nn}}{h_0}. \quad (3.21)$$

Just as the solid modeler was used to calculate the penetration between contacting tissue layers, it can also be used to calculate the undeformed tissue layer thickness, h_0 .

Finally, in order to complete the normal elastic stress calculation, the in-plane tangential components of solid strain are needed. These strain components can be calculated using the finite element shape functions presented in Eqn. (3.17). The layer apportioned proximity data is, again, assumed to be the solid displacement. Therefore, using the standard method of calculating finite element strains [13; 32], as was done in the ν - p formulation of Chapter 2, the tangential components of strain can be calculated:

$$\boldsymbol{\epsilon}^s = \frac{1}{|J|} \left(\nabla \mathbf{N}(\boldsymbol{\xi}) \right)_{sym} \mathbf{d}_n^s = \frac{1}{|J|} \mathbf{D}_\epsilon(\boldsymbol{\xi}) \boldsymbol{\zeta}_n \quad (3.22)$$

where J is the Jacobian determinant and is calculated as:

$$|J| = \frac{\partial t_1}{\partial \xi_1} \frac{\partial t_2}{\partial \xi_2} - \frac{\partial t_2}{\partial \xi_1} \frac{\partial t_1}{\partial \xi_2} . \quad (3.23)$$

The matrix \mathbf{D}_ϵ used to calculate the in-plane strains can be either two dimensional (for a three dimensional problem) or one dimensional (for a two dimensional problem) as the in-plane strains are only calculated on a surface of the overall model, one dimension lower than the total dimensionality of the problem.

3.3.2 Calculation of Total Stress from Proximity Data

To calculate the normal total traction from proximity data, the proportionality constant, γ , must be calculated via Eqn. (3.15) (see Section 3.2.3). The magnitude of the total force is the square root of the sum of the squares of it's components:

$$|\mathbf{F}^{Total}| = \sqrt{\sum_{i=1}^3 \left(F_i^{Total} \right)^2} . \quad (3.24)$$

To perform the integral in the denominator of Eqn. (3.15) a 3-point numerical integration rule [13; 32] will be used with the 6-node triangular mesh on the contact surface. This results in:

$$\int_{\Gamma^c} g_i n_i d\Gamma = \int_{\Gamma^c} \left(\sum_{i=1}^2 \sum_{a=1}^6 N_a d_{ia} n_i \right) d\Gamma = \sum_{b=1}^3 \left(\sum_{a=1}^6 N_a(\xi_b) d_{ia} n_i \right) W_b |J|, \quad (3.25)$$

where $N_a(\xi_b)$ are the finite element shape functions evaluated at the numerical integration stations, W_b are the weights for the 3-point rule and $|J|$ is the determinant of the Jacobian matrix.

With these two equations the parameter γ can be calculated, and in turn, the total normal traction at any point on the contact surface. Combined with the previous calculation for the normal elastic traction, ϕ^* can be calculated pointwise over the contact surface. Using ϕ^* , nodal values for pressure and total traction (v-p elements) or solid and fluid traction (mixed-penalty elements) can be calculated through the use of Eqns. (3.1) - (3.5) and applied as boundary conditions for analysis. These boundary conditions will be appropriate for approximating biphasic contact, as will be demonstrated in the next chapter.

Chapter 4: Validation Examples: Axisymmetric Contact Problems

In order to validate the proximity method presented in the last chapter, axisymmetric models that can be analyzed with both biphasic finite element formulations discussed in Chapter 2 (2D mixed-penalty contact and 3D velocity-pressure with the proximity derived boundary conditions) are used. The goal of this chapter is to demonstrate that the proximity method gives comparable results to those seen in an independent biphasic contact analysis and to demonstrate the accuracy of the following assumptions, made during development of the method:

- the layer-partitioned proximity is a good measure of normal displacement, and therefore solid strain, in a contact problem.
- the assumptions made in calculating the normal elastic traction and the normal total traction result in accurate calculations of the traction values.

For the present application, the above assumptions are made for the short time response of biphasic tissues. It is these physiologically relevant times that are important for the type of diarthrodial joint analysis that this method is intended to be used for.

4.1 Axisymmetric Validation Model Description

The method will be validated for the short-time response of a canonical problem whose geometry and properties approximate those of the human shoulder. In the

canonical joint problem, depicted in Figure 4.1, two biphasic layers, shown as the shaded areas, are attached to rigid bodies, representing the subchondral bone. A force is applied in the axial (z) direction to the upper rigid layer over a linear 0.1 second ramp, then held constant for the remaining 0.1 second over which this validation analysis is conducted. This type of loading is chosen to simulate a time frame that is representative of a physiological time that a joint would be at a single static position during an articulation.

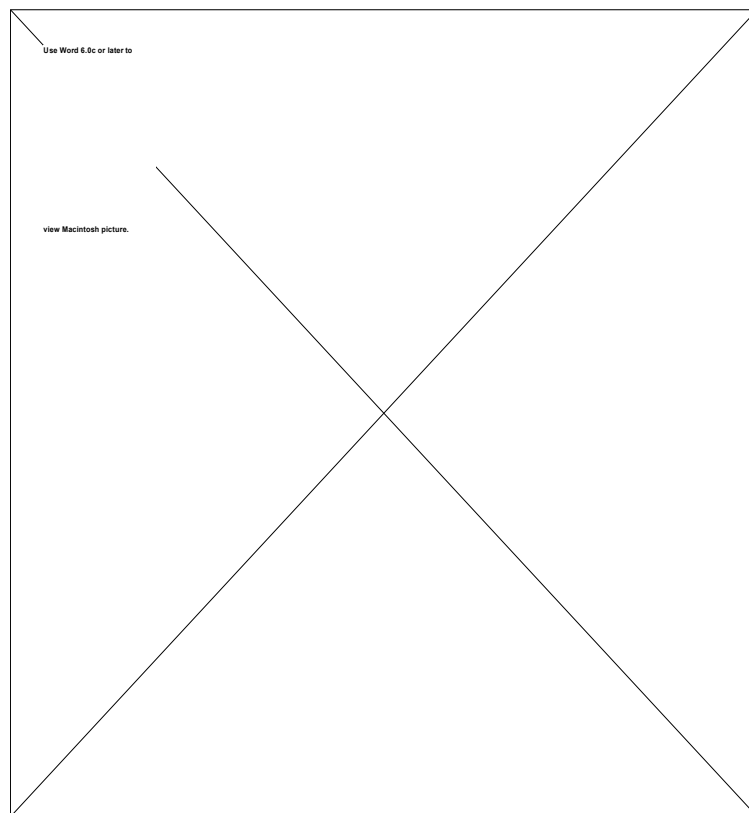


Figure Chapter 4: .1 Canonical Joint Model Configuration

The configuration is analyzed for four geometric cases, where the congruency, curvature and tissue thickness are varied so that their effects on the proximity results may be observed. The congruency is defined as:

$$\frac{1}{R_1} - \frac{1}{R_2} = \frac{1}{\text{congruency}}, \quad (4.1)$$

where values for R_1 and R_2 for the four cases are given in the Table 4.1.

Case Name	R_1 (mm)	R_2 (mm)	w (mm)	h_1 (mm)	h_2 (mm)	F (N)
G1	323.0	∞	15.0	1.0	1.0	75.0
G2	650.0	∞	15.0	1.0	1.0	75.0
G3a	25.0	26.0	15.0	1.0	1.0	75.0
G3b	25.0	26.0	15.0	0.75	1.5	75.0

Table Chapter 4: .1 Canonical Joint Dimensions

For each validation case, a 2D contact analysis is first performed using the biphasic contact finite element analysis of Donzelli [10]. Three dimensional representations of these axisymmetric configurations are then constructed using the solid modeler with the dimensions given above. In these validation cases, the solid modeler is used to interpenetrate the opposing tissue layers. It is therefore necessary to define the maximum value of penetration in order to generate the 3D proximity data. For this study, the calculated axial displacement of the upper rigid body (see Figure 4.1) from the 2D contact analysis is applied within the solid modeler to the 3D solid model of layer 1, allowing it to rigidly penetrate the model of layer 2. This approximates the stereophotogrammetry process, where the joint kinematics are measured for the rigid

bones. Proximity data is then calculated within the solid modeler for each layer exactly as it would be for models defined via SPG.

Three sets of isotropic material properties (see Table 4.2) are chosen for the tissue layers of Figure 4.1, from which three material configurations are selected for analysis (see Table 4.3).

Material	H_A (MPa)	λ (MPa)	ϕ^s	ν	κ (m⁴/Ns)
M1 (Rigid)	6905	338.9	0.25	0.05	3.0×10^{-18}
M2 (Biphasic 1)	0.56	0.0294	0.25	0.05	1.7×10^{-15}
M3 (Biphasic 2)	0.20	0.01053	0.17	0.05	5.0×10^{-15}

Table Chapter 4: .2 Canonical Joint Material Property Sets

Material Configuration	Layer 1 / Layer 2
MC1	M1 / M2
MC2	M2 / M2
MC3	M2 / M3

Table Chapter 4: .3 Canonical Joint Material Configurations

The previously defined geometric configurations in Table 4.1 and the material configurations in Table 4.3 are combined to give the following 12 analysis cases:

Analysis Case	Geometric & Material Configurations		
A1 - A3	G1 & MC1	G1 & MC2	G1 & MC3
A4 - A6	G2 & MC1	G2 & MC2	G2 & MC3
A7 - A9	G3a & MC1	G3a & MC2	G3a & MC3
A10-A12	G3b & MC1	G3b & MC2	G3b & MC3

Table Chapter 4: .4 Canonical Joint Analysis Cases

These cases are defined such that the effects of joint congruency, tissue layer curvature and tissue layer thickness on the accuracy of the proximity method can be investigated. Each analysis case is run with the 2D biphasic contact software and the calculations of Chapter 3 are done in two dimensions on the same meshes using the numerical methods that are outlined in Section 3.3 in order to validate the bulleted points at the beginning of this chapter. Case A12 is also completed with the 3D proximity software, in order to compare the overall results to the contact solutions.

4.2 Finite Element Configurations

The geometric models defined in Figure 3.1 and Table 3.1 are discretized into finite element meshes for both the 2D contact analyses and the 3D proximity analyses. Representative meshes for geometric case G3b are shown below.

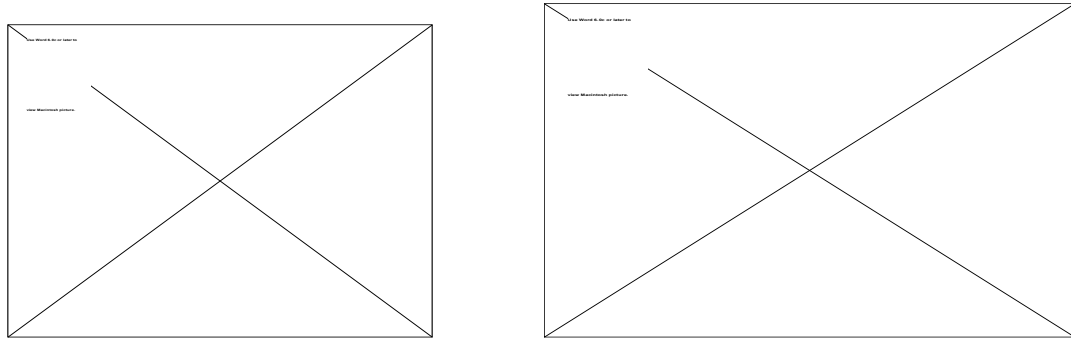


Figure Chapter 4: .2 Representative FE Meshes of Canonical Joint Model for 2D

Contact (left) and 3D Proximity (right) Analyses

The meshes shown in Figure 4.2 have 884 elements and 9,083 free d.o.f. (2D case, shown on the left) and 5,817 elements and 26,071 free d.o.f. (3D case, layer 2, shown on the right). In the 3D analysis, the tissue-bone interface is modeled as rigid and impermeable. Each of the analysis cases defined in Table 4.4 was run on a Sun Ultra Sparc workstation.

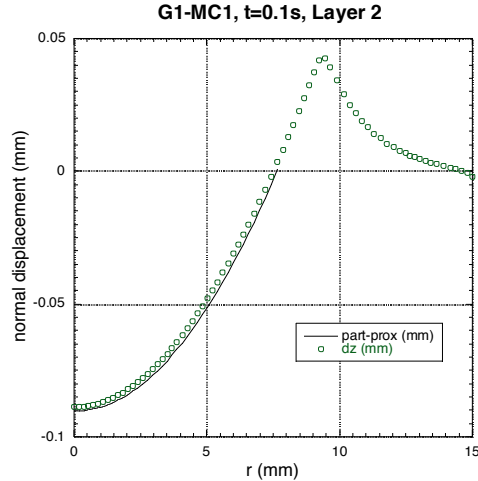
4.3 Results

In this section, results for a representative cross-section of the analysis cases of Table 4.4 will be presented. These cases demonstrate the types of results that are seen for all of the analysis cases. In order to validate the method presented in Chapter 3, plots of solid displacement and apportioned proximity data, elastic part of the solid stress, and total stress for the 2D contact analyses and the 3D proximity analyses will be presented for comparison. Final values of ϕ^* are tabulated for the 2D and 3D analyses and the error introduced from the proximity method is calculated. Full field results for

two of the cases in Table 4.4 will be presented in order to demonstrate the agreement in the overall solution and to demonstrate the usefulness of the proximity method.

4.3.1 Two-dimensional Validations

Following the development of the proximity method given in Chapter 3, the first quantity to be calculated is the layer apportioned proximity data. The plots in Figure 4.3 show a comparison of the total proximity data, the layer assigned proximity data and the normal displacement at the contact surface calculated with the biphasic contact code, for a representative number of the analysis cases. For the cases that use material configuration MC1, only results for Layer 2, the deformable layer of Figure 4.1, are shown.



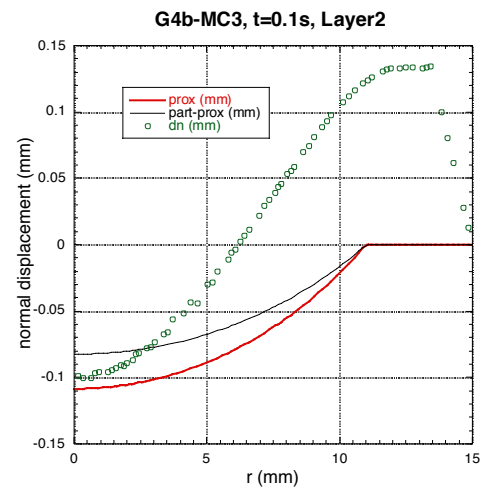
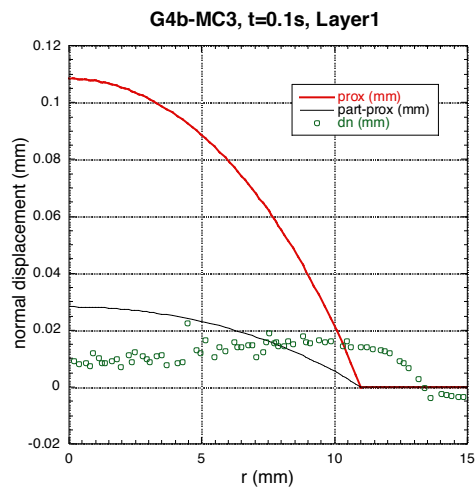
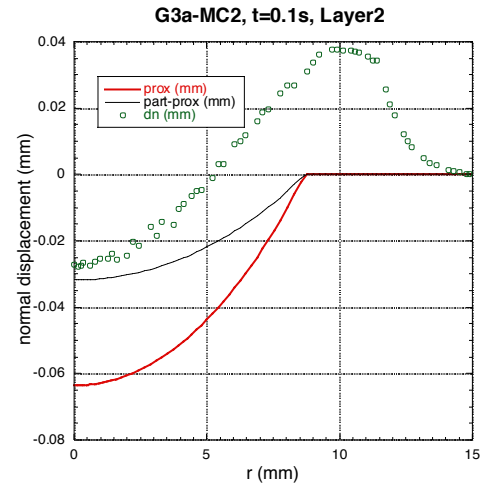
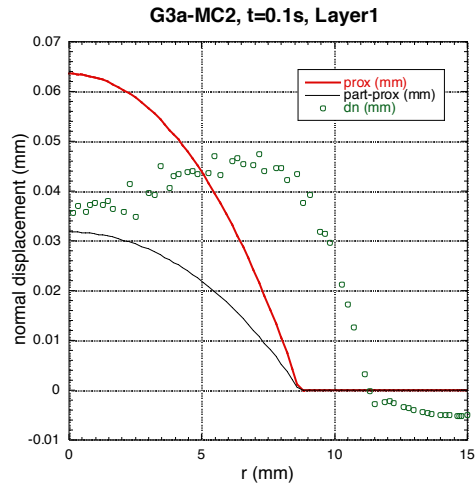
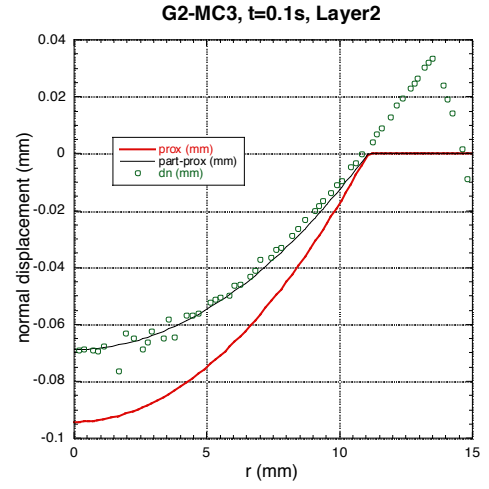
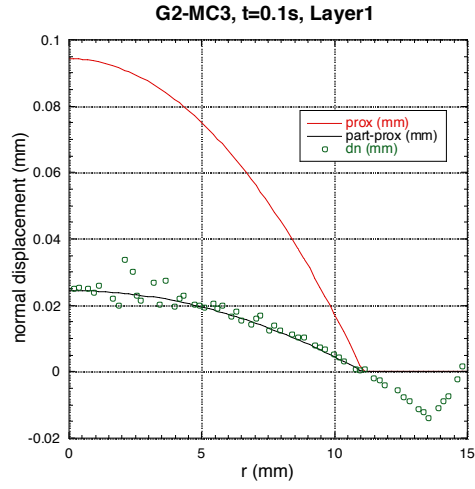
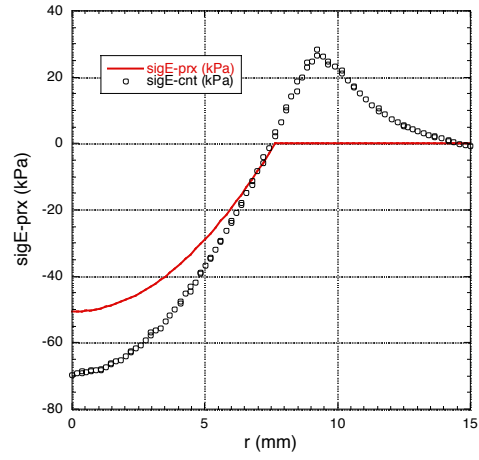


Figure Chapter 4: .3 Normal displacement, total proximity, and layer assigned proximity vs. radial position at $t=0.1s$

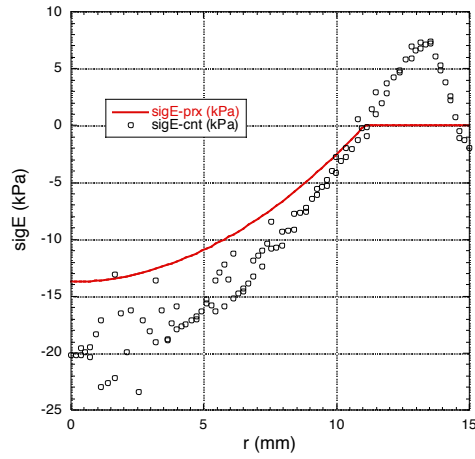
The symbols in the Figs. 4.3 are the nodal values of tissue deformation calculated by the 2D contact code. The solid lines are the total proximity and the proximity that has been reduced by the layer apportioning factor, α (Eqn. (3.19)). It can be seen from these plots that the cases in which Layer 2 (Figure 4.1) is flat, $R_2=\infty$, the layer assigned proximity can almost exactly predict the normal displacement from the contact analyses. In the cases where both layers are curved (more typical of real joint analysis) the proximity method does not perform as well for predicting the normal displacement. This is because of the initial smaller separation of the layers, or the greater congruency of the model. When the tissue layers of these models deform the initial separation is quickly filled in, resulting in a greater contact area. The contact area in the proximity method is static, and cannot account for this effect. However, the layer assigned proximity data does still follow the general trends of the contact displacements for these cases and, as will be shown below, can still produce acceptable results for the various stress calculations that are needed.

Figures 4.4 are a comparison of the normal component of elastic solid stress for the two methods along the contact surface. The symbols are calculated nodal values from the 2D contact code and the solid lines are the values calculated via the proximity method using the displacements shown in Figure 4.3 (Eqns. (3.6) - (3.12)).

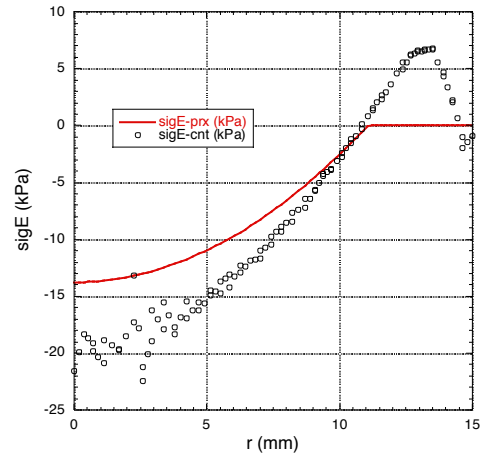
G1-MC1, t=0.1s, Layer2



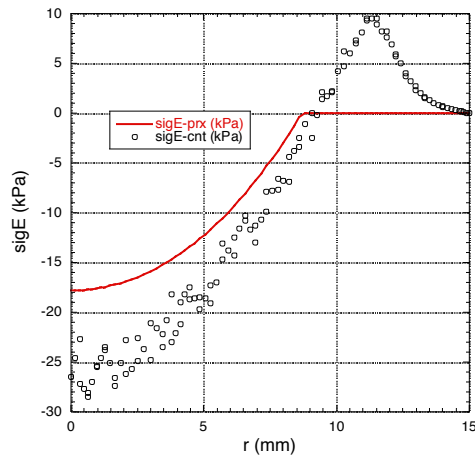
G2-MC3, t=0.1s, Layer1



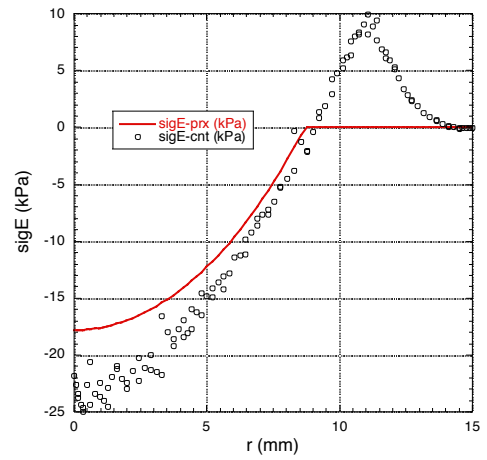
G2-MC3, t=0.1s, Layer2



G3a-MC2, t=0.1s, Layer1



G3a-MC2, t=0.1s, Layer2



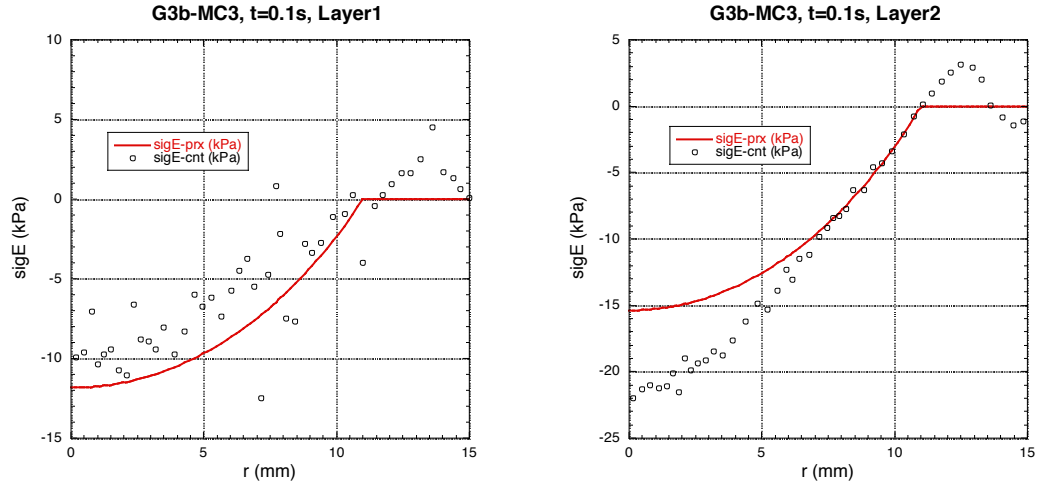
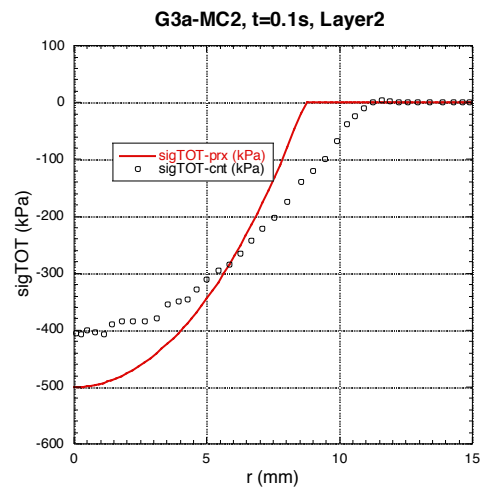
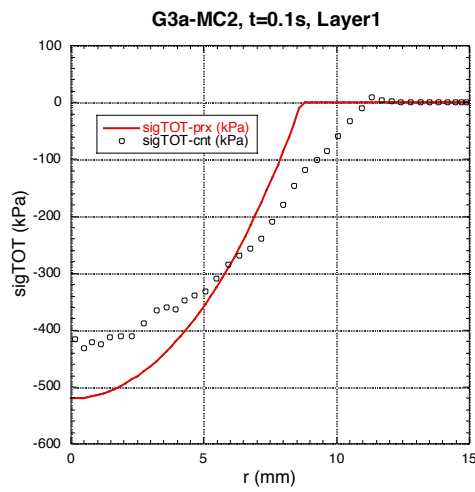
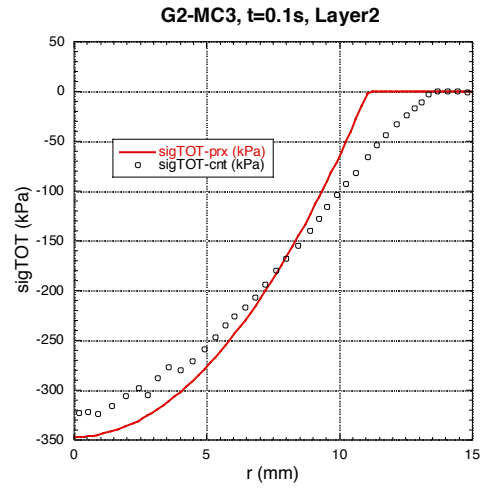
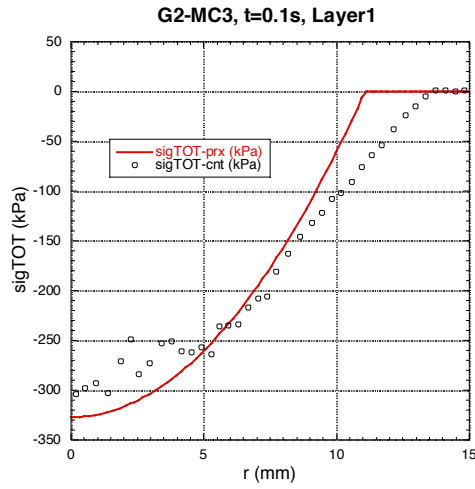
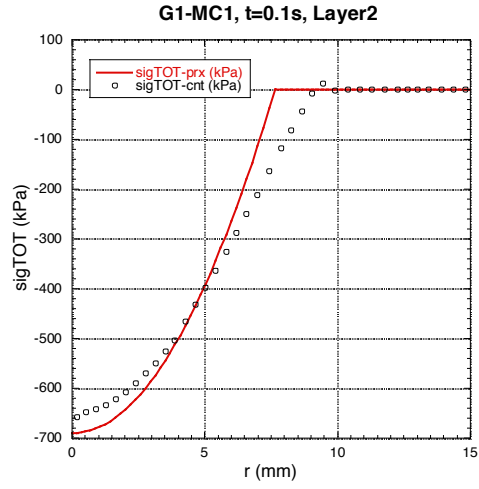


Figure Chapter 4: .4 Normal elastic stress for contact and proximity analyses vs. radial position at the contact surface at $t=0.1s$

The plots of Figure 4.4 show that while the displacement results of Figure 4.3 were not always ideal, the normal elastic stress calculation still produces accurate results. However, the effect of underestimating the contact surface can still be seen in these plots. The biphasic contact analyses produce a tensile stress near the edge of the contact surface, but the proximity method is unable to predict any values outside of the contact area as the proximity data is not defined outside of this surface. While this may be a concern for the full-field results presented later in the chapter, the ϕ^* calculation, which is performed over the contact surface should not be effected.

Finally, to complete the ϕ^* calculation, values for the normal total traction are needed. Figure 4.5 shows line plots of these values calculated over the contact surface for both methods. The symbols represent the values from the contact code, the solid lines are the values calculated by the proximity method.



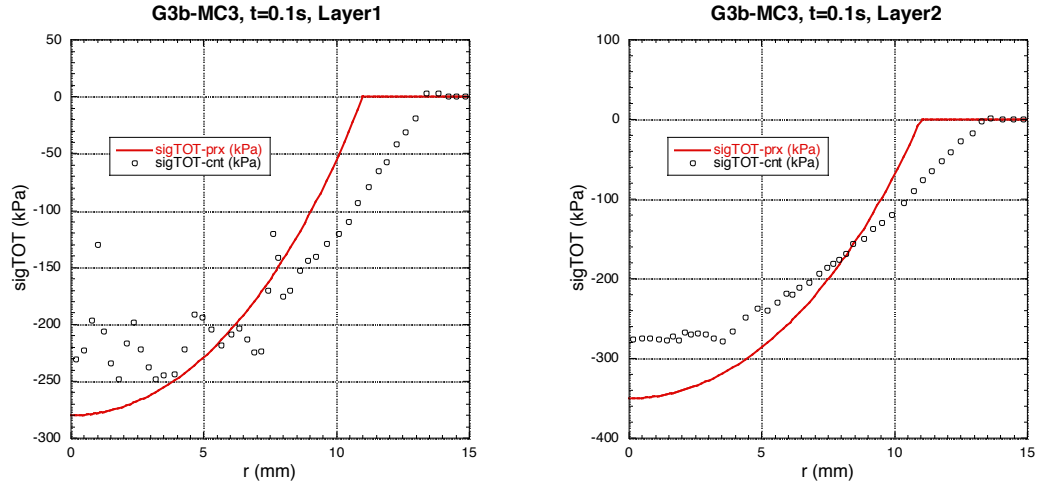


Figure Chapter 4: .5 Normal total stress for contact and proximity analyses vs. radial position at the contact surface at t=0.1s

Once again, as with the other plots, the effect of underestimating the contact area is seen. For the normal total traction the result is an elevated peak stress in the proximity method as the same total load that is applied in the contact analysis is being supported by a smaller surface in the proximity method. However, the proximity method is again able to closely follow the trends displayed by the contact analysis.

With the quantities shown in the above plots, final values of ϕ^* can be calculated. Table 4.5 summarizes the values from both methods on the two tissue layers. The error between the two methods is also tabulated.

	A1	A2	A3	A4	A5	A6
2D Layer1	NA	0.312	0.303	NA	0.300	0.293
3D Layer1	NA	0.324	0.293	NA	0.324	0.318
% Error	-	3.7%	3.3%	-	7.4%	7.8%
2D Layer2	0.329	0.303	0.243	0.294	0.293	0.213
3D Layer2	0.308	0.324	0.222	0.324	0.271	0.194
% Error	3.3%	6.4%	8.6%	9.3%	7.5%	8.9%

	A7	A8	A9	A10	A11	A12
2D Layer1	NA	0.292	0.287	NA	0.273	0.261
3D Layer1	NA	0.326	0.322	NA	0.254	0.284
% Error	-	10.4%	10.9%	-	6.9%	8.1%
2D Layer2	0.297	0.292	0.204	0.315	0.332	0.183
3D Layer2	0.312	0.267	0.187	0.333	0.304	0.214
% Error	4.8%	8.6%	8.3%	5.4%	8.4%	14.5%

Table Chapter 4: .5 Average ϕ^* values for 2D contact and 3D proximity analysis cases

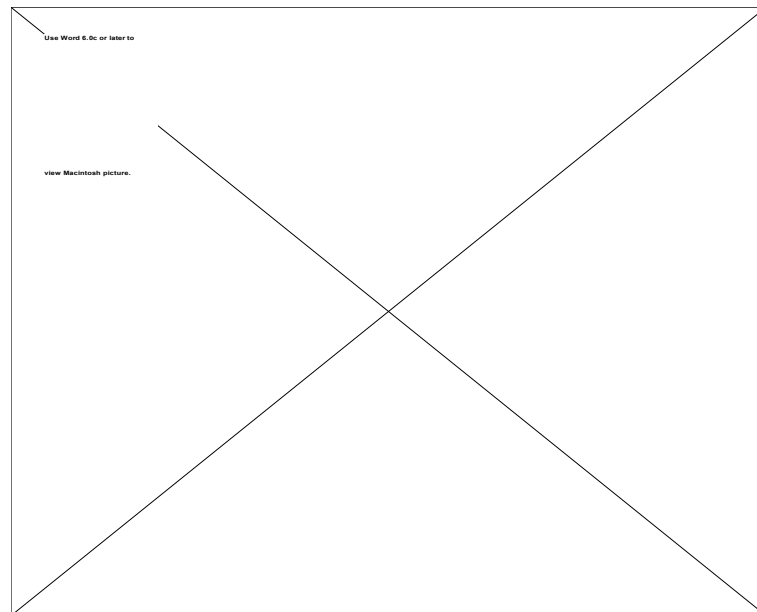
The average error in Table 4.5 is 7.6%. Given the assumptions that were made in Chapter 3, this is an acceptable amount of error. Again, it can be seen that the error for the cases with a flat Layer 2 is lower than the more congruent cases. This appears to be the major contributor to any error that is introduced by the proximity method. By comparing cases A7-A9 with cases A10-A12 it can be seen that the change in tissue

thickness did not have any significant effect on the results. The same is true when comparing the different material models. For example, comparison of case A8 and case A9 shows that using different materials for each of the layers in the same model did not increase the error in the ϕ^* calculation. While the calculations have proven to be adequate, the full field response of a problem must be investigated to gauge the true usefulness of the proximity method.

4.3.2 Comparison of 2D and 3D Results

To demonstrate the similarities in derived quantities such as stress and strain, full field results are presented in this section for both the 2D biphasic contact code and the 3D proximity method for analysis case A12 of Table 4.4.

The first quantity investigated is the strain in the z-direction. Figure 4.6 shows contour plots of this strain for both tissue layers, completed by both analysis methods.



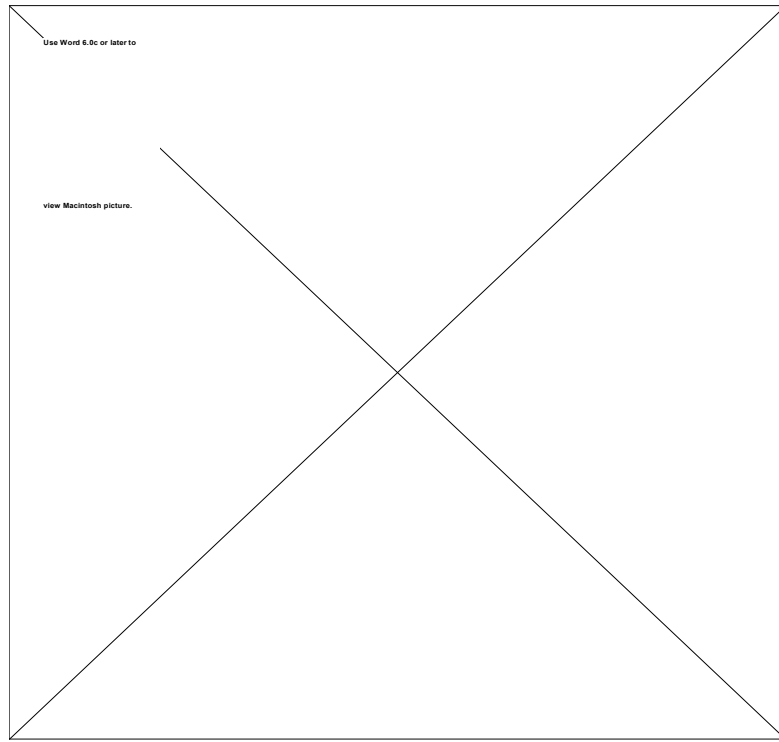


Figure Chapter 4: .6 2D (upper) and 3D (lower) normal solid strain for analysis case

A12

The next quantity is the solid strain on the r-z face. This is the plane of symmetry that is seen facing outward in the following figure.

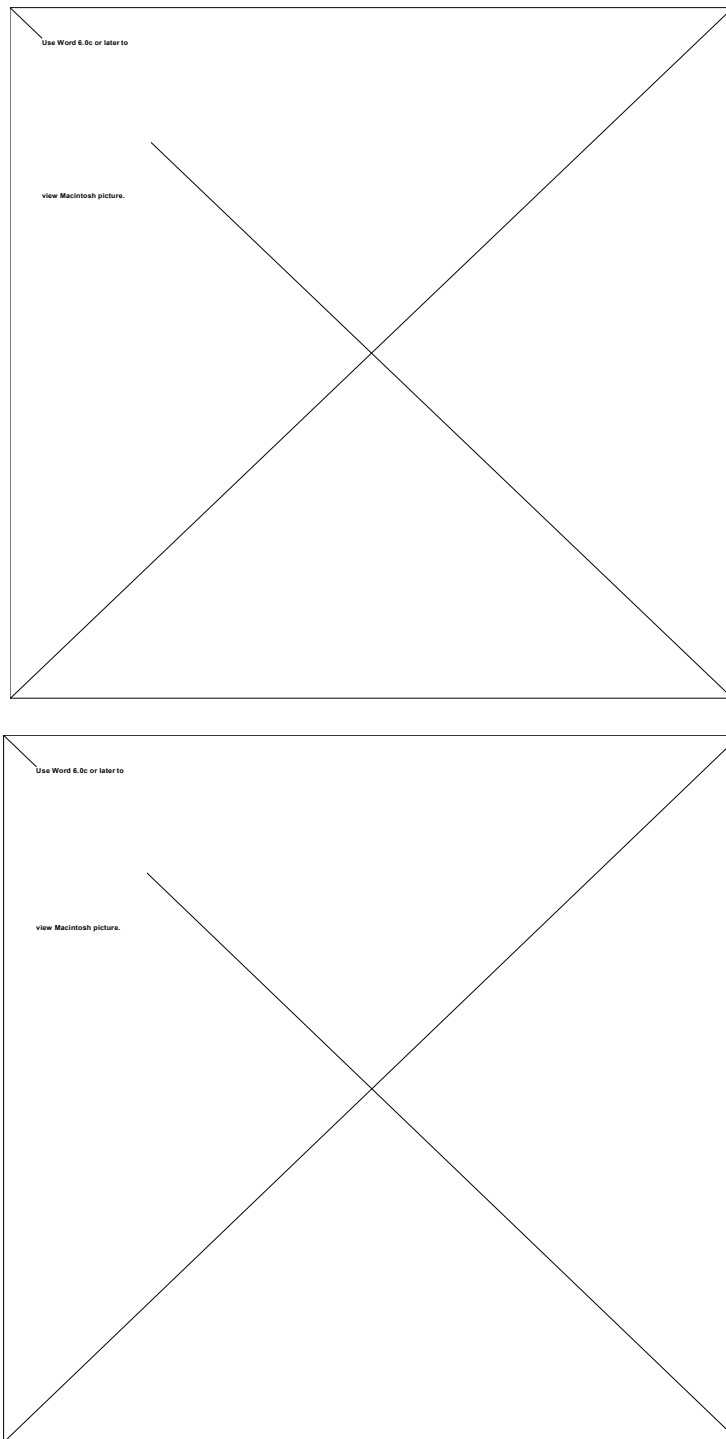


Figure Chapter 4: .7 2D (upper) and 3D (lower) solid strain on z-r face for analysis

case A12

Figures 4.6 & 4.7 show that the strain results give good agreement in both magnitude and the pattern of the strain distributions. As was seen in the line plots above, the effect of the smaller contact area can be seen in Figures 4.6 & 4.7. Near the outer limit of the radial direction, where the strain values approach zero, the 2D contact solution holds its non-zero values of strain over a greater distance, while the strain in the 3D proximity solution dies off before it reaches the periphery of the model. This is a direct result of the smaller contact area. Despite this, the results still look very similar, and it can be seen how these types of visualizations could be of use to researchers trying to understand the three dimensional response of biphasic soft tissues to physiological loading.

Chapter 5: Summary and Conclusions

In this thesis a method for approximating biphasic tissue contact has been developed and implemented. This method reduces the computational complexity of three dimensional contact analysis by replacing contacting bodies with appropriate surface tractions. These surface tractions are derived from proximity data, which is calculated from geometric data for the biphasic tissues, obtained, for example through stereophotogrammetry, and solid modeling techniques. The linear biphasic theory is used to convert the proximity data into traction boundary conditions for finite element analysis of the individual layers. Results were presented for canonical joint problems that are axisymmetric and can be completed in both two and three dimensions. These results show good agreement between the proximity method and biphasic contact analysis and give confidence to carry forward with physiological problems where complex models derived from stereophotogrammetry are used.

The validation examples demonstrate that the proximity method gives a good approximation to biphasic contact over early response times. The assumption that proximity data can be used as an approximation to surface deformation from contact analysis proved to be accurate. This led to an acceptable calculation of normal elastic traction using strain-displacement and stress-strain laws. The method of balancing the total applied force with the total normal traction by integrating over the contact surface also proved to be adequate. This all led to accurate calculations of the load partitioning factor, ϕ^* . There are some obvious shortcomings with the proximity method, but the

qualitative and quantitative properties of the three dimensional analyses completed with the proximity method show that it is capable of being used by researchers to gain insight into diarthrodial joint mechanics while full three dimensional contact is being developed. One of the attractive properties of the proximity method is it's ability to reduce the computational resources needed to do three dimensional contact analysis. The proximity method will always hold this advantage over full 3D contact analysis, which is important for those who don't have access to large scale computing resources. Further, once 3D contact analysis is developed, the present method can also be validated on 3D diarthrodial joint cases using SPG and joint kinematic data. This will perhaps show the proximity method to be a viable (as well as computationally advantageous) alternative to 3D contact over some range of analysis times or certain specific geometric or material cases.

The most apparent shortcoming for the method is that it cannot completely predict the contact areas in opposing tissue layers. This is due to the physics of biphasic contact problems. As the tissues come into contact they deform outward at the edge of contact and therefore generate an even larger contact surface. The proximity data is derived by allowing the bodies to rigidly interpenetrate, not accounting for deformation of the contact surface. The end result is that the applied load (which is accurately calculated via static equilibrium) acts over a smaller area, increasing the levels of stress and strain under the contact surface. However, these elevated values are not significant, as shown in Section 4.3.2, and the results remain very similar. These slightly elevated

strains are also predictable and should be taken into account when analyzing soft tissues with this method.

There are a few ways in which the method can be extended in the future. First, the calculations can be made more efficient, and perhaps, made more accurate. It can be seen from the plots in Chapter 4 that the ϕ^* parameter loses resolution near the periphery of the contact area. A scheme for picking optimal sample points in the interior of the contact face and averaging their calculated results could give a more accurate calculation of ϕ^* . Also, the one dimensional approximation of α given in Eqn. (3.19) could be eliminated and the entire multi-dimensional (2D or 3D) calculation could be done. The total proximity, g^{Total} , would have to be differentiated, but this could be done with the same methods used to differentiate the layer-assigned proximity given in Eqn. (3.22). These calculations will be more accurate, but more time consuming, and thus it should be emphasized that for the present implementation, both of these simplified calculations have proven adequate to produce results that are in good agreement with the biphasic contact results.

An intriguing extension of the method is to problems in which the proximity boundary conditions are “swept” over a tissue layer to simulate full joint articulation. There are a few technical issues that need to be addressed before this would be possible. First, it needs to be verified that removing a proximity-derived load from a tissue layer results in the tissue layer returning to its original, undeformed state in a predictable manner. This is necessary as the load will at one instant be applied to a portion of the tissue surface and will not at the next instant in time. Also, a geometric modeling

technique to identify the entire area of the articulating surface that may be in contact at some point during the analysis must be developed. This is necessary for mesh refinement and also for the application of analysis attributes.

Another extension of the method will be to non-linear problems and other types of finite element formulations (mixed-penalty and hybrid, for example). As was mentioned earlier, the deformations that take place in cartilage are known to be large, exceeding the limits of the linear theory. While the linear theory provides accurate approximations for low loads, the non-linear theory is needed to fully quantify cartilage mechanics. The proximity method should apply equally well to non-linear and linear problems. Also, the velocity-pressure formulation was utilized in this study for the three dimensional problems, but there will almost certainly be advances in biphasic finite element formulations in the future. Following the derivations in Chapter 3 the proximity method should similarly apply to these any type of biphasic formulation.

With confidence in the method, three dimensional problems where the geometry is derived from stereophotogrammetry can now be completed. This class of problems will be the first to utilize a robust material model, like the biphasic theory, with accurate tissue representations to give a representative picture of the mechanical state of hydrated soft tissues under physiological loads. Future work will include a study of physiological tissue layers, possibly of the shoulder or knee, using the proximity-derived boundary conditions. This type of information can eventually aid clinicians in their treatment of patients and researchers in their efforts to understand joint mechanics and disease.

Bibliography

1. Almeida, E. S. (1995). Finite Element Formulations for Biological Soft Hydrated Tissues Under Finite Deformation. PhD Thesis. Mechanical Engng, Aeronautical Engng and Mechanics. Troy, NY, Rensselaer Polytechnic Institute.
2. Almeida, E. S. and Spilker, R. L. (1997). "An evaluation of mixed and penalty biphasic elements using the linear confined compression problem." International Journal for Numerical Methods in Engineering (**in review**):
3. Almeida, E. S. and Spilker, R. L. (1997). "Finite element formulations for hyperelastic transversely isotropic biphasic soft tissues." Computer Methods in Applied Mechanics and Engineering (**in press**):
4. Almeida, E. S. and Spilker, R. L. (1997). "Mixed and penalty finite element models for the nonlinear behavior of biphasic soft tissues in finite deformation: Part I - Alternate formulations." International Journal for Computer Methods in Biomechanics and Biomedical Engineering (**in press**):
5. Almeida, E. S. and Spilker, R. L. (1997). "Mixed and penalty finite element models for the nonlinear behavior of biphasic soft tissues in finite deformation: Part II - Nonlinear examples." International Journal for Computer Methods in Biomechanics and Biomedical Engineering (**in press**):
6. Ateshian, G. A., Soslowsky, L. J. and Mow, V. C. (1991). "Quantitation of articular surface topography and cartilage thickness in knee joints using stereophotogrammetry." Journal of Biomechanics **24**(8): 761-776.
7. Cohen, B., Gardner, T. R. and Ateshian, G. A. (1993). The influence of transverse isotropy on cartilage indentation behavior -- A study of the human humeral head. Transactions Orthopaedic Research Society . Chicago, ORS. 185.
8. Donzelli, P. S. (1995). A Mixed-Penalty Contact Finite Element Formulation for Biphasic Soft Tissues. PhD Thesis. Mechanical Engineering, Aeronautical Engineering and Mechanics. Troy, NY, Rensselaer Polytechnic Institute.
9. Donzelli, P. S. and Spilker, R. L. (1996). A finite element investigation of solid phase transverse isotropy in contacting biphasic cartilage layers. 1996 Advances in Bioengineering Ed. S. Rastegar. New York, ASME. 349.
10. Donzelli, P. S. and Spilker, R. L. (1997). "A contact finite element formulation for biological soft hydrated tissues." Computer Methods in Applied Mechanics and Engineering (**accepted for publication**):
11. Holmes, M. H. (1986). "Finite deformation of soft tissue: Analysis of a mixture model in uni-axial compression." Journal of Biomechanical Engineering **108**: 372-381.

12. Hou, J. S., Holmes, M. H., Lai, W. M. and Mow, V. C. (1989). "Boundary conditions at the cartilage-synovial fluid interface for joint lubrication and theoretical verifications." Journal of Biomechanical Engineering **111**(1): 78-87.
13. Hughes, T. J. R. (1987). The Finite Element Method: Linear Static and Dynamic Analysis. Englewood Cliffs, Prentice-Hall, Inc.
14. Lai, W. M., Hou, J. S. and Mow, V. C. (1991). "A triphasic theory for the swelling and deformational behaviors of articular cartilage." Journal of Biomechanical Engineering **113**(3): 245-258.
15. Lai, W. M. and Mow, V. C. (1980). "Drag-induced compression of articular cartilage during a permeation experiment." Biorheology **17**: 111-123.
16. Mish, K. D., Herrmann, L. R. and Muraleetharan, K. (1992). A comparison of Biot formulation finite element models for two- and three-dimensional transient soil problems. Symposium on Computational Mechanics of Porous Materials and their Thermal Decomposition, Tempe, Arizona, ASME.
17. Mow, V. C., Hou, J. S., Owens, J. M. and Ratcliffe, A. (1990). Biphasic and quasilinear viscoelastic theories for hydrated soft tissues. Biomechanics of Diarthrodial Joints Eds. V. C. Mow, A. Ratcliffe and S. L.-Y. Woo. 215-260.
18. Mow, V. C., Kuei, S. C., Lai, W. M. and Armstrong, C. G. (1980). "Biphasic creep and stress relaxation of articular cartilage in compression: theory and experiments." Journal of Biomechanical Engineering **102**: 73-84.
19. Mow, V. C. and Mak, A. F. (1985). Lubrication of diarthrodial joints. Handbook of Bioengineering Eds. Skulak and Chien. McGraw-Hill.
20. Mow, V. C., Ratcliffe, A. and Poole, A. R. (1992). "Cartilage and diarthrodial joints as paradigms for hierarchical materials and structures." Biomaterials **13**: 67-97.
21. Mow, V. C., Zhu, W. and Ratcliffe, A. (1991). Biomechanical properties of articular cartilage and the meniscus. Basic Orthopaedic Biomechanics Eds. V. C. Mow and W. C. Hayes. New York, Raven Press.
22. O'Bara, R. M., Shephard, M. S. and Ateshian, G. A. (1995). Geometric model construction and mesh generation for soft tissues in joints. Proceedings of the 1995 Bioengineering Conference Eds. R. M. Hochmuth, N. A. Langrana and M. S. Hefzy. New York, ASME. 215-216.
23. Oomens, C. W. J. and Van Campen, D. H. (1987). "In vitro compression of a soft tissue layer on a rigid foundation." Journal of Biomechanics **20**(10): 923-935.
24. Oomens, C. W. J., Van Campen, D. H. and Grootenboer, H. J. (1987). "A mixture approach to the mechanics of skin." Journal of Biomechanics **20**(9): 877-885.
25. Shephard, M. S. and Georges, M. K. (1991). "Automatic three-dimensional mesh generation by the finite octree technique." International Journal for Numerical Methods in Engineering **32**: 709-739.

26. Simon, B. R., Wu, J. S. S., Zienkiewicz, O. C. and Paul, D. K. (1986). "Evaluation of U-W and U-P finite element methods for the dynamic response of saturated porous media using one-dimensional models." International Journal for Numerical and Analytical Methods in Geomechanics **10**: 483-499.
27. Soslowsky, L. J., Ateshian, G. A. and Mow, V. C. (1990). Stereophotogrammetric determination of joint anatomy and contact areas. Biomechanics of Diarthrodial Joints Eds. V. C. Mow, T. A. Ratcliffe and S. L.-Y. Woo. Springer-Verlag. 243-268.
28. Spilker, R. L. and Maxian, T. A. (1990). "A mixed-penalty finite element formulation of the linear biphasic theory for soft tissues." International Journal for Numerical Methods in Engineering **30**: 1063-1082.
29. Suh, J.-K., Spilker, R. L. and Holmes, M. H. (1991). "A penalty finite element analysis for nonlinear mechanics of biphasic hydrated soft tissue under large deformation." International Journal for Numerical Methods in Engineering **32**: 1411-1439.
30. Vermilyea, M. E. and Spilker, R. L. (1992). "A hybrid finite element formulation of the linear biphasic equations for soft hydrated tissues." International Journal for Numerical Methods in Engineering **33**: 567-594.
31. Wayne, J. S., Woo, S. L.-Y. and Kwan, M. K. (1991). "Application of the u-P finite element method to the study of articular cartilage." Journal of Biomechanical Engineering **113**(4): 397-403.
32. Zienkiewicz, O. C. and Taylor, R. L. (1989). The Finite Element Method. London, McGraw-Hill Book Company.